A simple method to simulate thermo-hydro-mechanical processes in leakoff-dominated hydraulic fracturing with application to geological carbon storage

Xin Ju, Pengcheng Fu*, Randolph Settegast, Joseph Morris

Atmospheric, Earth, and Energy Division, Lawrence Livermore National Laboratory, Livermore, CA 94550 USA.

*Corresponding author: fu4@llnl.gov

Abstract: A potential risk of injecting CO_2 into storage reservoirs with marginal permeability ($\lesssim 10^{-14}$ m^2) is that commercial injection rates could induce fracturing of the reservoir and/or the caprock. Such fracturing is essentially fluid-driven fracturing in the leakoff-dominated regime. Recent studies suggested that fracturing, if contained within the lower portion of the caprock complex, could substantially improve the injectivity without compromising the overall seal integrity. Modeling this phenomenon entails complex coupled interactions among the fluids, the fracture, the reservoir, and the caprock. We develop a simple method to capture all these interplays in high fidelity by sequentially coupling a hydraulic fracturing module with a coupled thermal-hydrological-mechanical (THM) model for nonisothermal multiphase flow. The model was made numerically tractable by taking advantage of self-stabilizing features of leakoff-dominated fracturing. The model is validated against the PKN solution in the leakoff-dominated regime. Moreover, we employ the model to study thermo-poromechanical responses of a fluid-driven fracture in a field-scale carbon storage reservoir that is loosely based on the In Salah

project's Krechba reservoir. The model reveals complex yet intriguing behaviors of the reservoir-caprock-fluid system with fracturing induced by cold CO_2 injection. We also study the effects of the *in situ* stress contrast between the reservoir and caprock and thermal contraction on the vertical containment of the fracture. The proposed model proves effective in simulating practical problems on length and time scales relevant to geological carbon storage.

Keywords: Geologic carbon storage, CO_2 fracturing, THM coupled modeling, multiphase multicomponent fluid flow, supercritical CO_2

1 Introduction

Geological carbon storage (GCS) is a promising measure to mitigate the effect of anthropogenic greenhouse gas emissions on climate change (Pacala and Socolow, 2004; International Energy Agency, 2010). To have a meaningful impact on the net CO_2 emission through GCS requires injecting a large quantity of CO_2 into subsurface geological reservoirs (Orr, 2009; Haszeldine, 2009). Existing pilot and experimental GCS projects mainly focus on storage reservoirs with ideal conditions, such as high porosity and high permeability (typically in the range of hundreds to thousands of millidarcy (1 mD = 10^{-15} m^2)). Considering that high quality reservoirs do not necessarily exist near CO_2 sources, the utilization of less favorable reservoirs, such as those with marginal permeabilities (i.e. low tens of mD), can significantly improve the commercial viability of CGS. In particular, recent commercial-scale field tests demonstrate that many such low permeability reservoirs have enormous CO_2 sources nearby and also enjoy easy access to drilling and comprehensive monitoring systems (Mito et al., 2008, Rinaldi et al, 2013). One good example of such sites is In Salah, Algeria, where a large amount of CO_2 source from nearby

natural gas production was injected into several storage reservoirs with marginal permeabilities (around 10 mD) (Iding and Ringrose, 2010; Rinaldi et al., 2013). Therefore, understanding CGS in reservoirs with marginal permeability is of great significance.

The main challenge facing injection into marginal-permeability reservoirs is the low injectivity under the pressure constraints that prevent fluid-driven fractures, namely, hydraulic fractures, from occurring in storage reservoirs. Previous studies showed that using a low injection rate that complies with the pressure constraint cannot achieve even a moderate commercial-level injection rate, i.e. a million-metric ton per year (Fu et al., 2017). However, recent studies postulated that the issue of low injectivity in marginal-permeability reservoirs might be effectively and safely mitigated if injection-triggered hydraulic fractures can be contained within reservoir rocks or the lower portion of the caprock without jeopardizing the overall seal integrity of the caprock complex (White et al., 2014; Fu et al., 2017). Circumstantial field data and observations from the In Salah site also suggest the possible existence of such postulated scenarios (Bohloli et al., 2017; Oye et al., 2013; White et al., 2014).

Modeling hydraulic fracturing in marginal-permeability GCS reservoirs entails the simulation of many complex processes: multiphase multicomponent fluid flow and heat transfer within fractures and matrix, mass and heat exchanges between fracture and matrix flows, poro/thermo-elastic deformation of solid rocks, and fracture propagation. Although many numerical studies have tackled this challenging task, significant simplifications had been made to mitigate various numerical challenges. These simplifications could be broadly divided into two groups: (1) treating hydraulic fractures as a highly permeable porous zone and (2) simplifying multiphase and nonisothermal flow behaviors of injected CO_2.

The first group of works typically simplify the dynamic interactions between fracture propagation and matrix flows and also neglect some key characteristics of hydraulic fractures (e.g. Morris et al., 2011; Pan et al., 2012; Raziperchikolaee et al., 2013; Sun et al., 2016). In other words, these are not designed to accurately predict the coupled thermo-hydro-mechanical (THM) responses of reservoir and caprocks once fluid-driven fractures are created. Many models in this category employ a continuum-based method, such as the dual porosity models and dual permeability models (e.g. Guo et al., 2017; Li and Elsworth 2019; Fan et al., 2019), neither of which could represent the complex flow behaviors associated with a propagating fracture. Moreover, works that attempt to capture geomechanical responses of hydraulic fractures often do not address complexities caused by an evolving fracture tip (e.g. Gor et al. 2014; Eshiet and Sheng 2014; Vilarrasa et al., 2014). In other words, they cannot explicitly depict the evolution of fracture extents and shapes which is critical to evaluating fracture containment (Rutqvist et al., 2016; Ren et al., 2017; Vilarrasa et al., 2017; Sun et al., 2017).

The second group of works, on the other hand, strive to capture essential features associated with hydraulic fracturing, such as fracturing propagation, seepage (leakoff) of fluid through fractures into reservoirs, and strong nonlinearity of the coupling between fracture permeability and hydraulic aperture (Fu et al., 2017; Culp et al., 2017; Salimzadeh et al., 2017; Salimzadeh et al., 2018; Gheibi et al. 2018; Mollaali et al., 2019; Yan et al., 2020), but substantially simplify fluid flow characteristics unique to supercritical CO_2 flow in a saline reservoir. The works of Fu et al. (2017) and Yan et al. (2020) focused on modeling isothermal fluid flow in porous media and ignored the thermal responses of fractures in the storage reservoir. However, these responses have a great impact on caprock integrity (Vilarrasa et al., 2014; Salimzadeh et al., 2018). The simulations conducted by Salimzadeh et al. (2018) used a surrogate flow model—single-phase

flow model— for simulating two-phase CO_2 flow, neglecting the pressure- and temperature-dependency of the PVT (pressure, volume, temperature) properties and multiphase flow of supercritical CO_2. In addition to discrete fracture models used by the above studies, smeared fracture models, such as the phase field method (Francfort and Marigo, 1998; Francfort et al., 2008), have also been adapted to address hydraulic fracturing related to CO_2 injection. Although it is straightforward to integrate the mass and energy conservations of CO_2 into the general formulation of the phase field method and to consider complex fracture processes (e.g. Culp et al., 2017; Mollaali et al., 2019), the smearing nature of this approach, nonetheless, poses stringent requirements on mesh refinement and adaptivity to accurately reconstruct the displacement discontinuities across the fracture surface (Lecampion et al., 2017). This numerical challenge has limited the application of the phase field to small-scale simulations (Mollaali et al., 2019). According to the latest review on the modeling of caprock integrity (Paluszny et al. 2020), a fully coupled 3D model that can capture the complex interplay among CO_2 injection, reservoir responses, and the propagation of hydraulic fractures at the field-scale is not currently available. The scarcity of such models is likely owing to the lack of a modeling scheme that can effectively and efficiently simulate the inherent complexity of hydraulic fracturing in marginal-permeability GCS reservoirs.

The objective of this study is to develop a modeling scheme that effectively and efficiently simulates hydraulic fracturing in GCS reservoirs and to study the mechanisms of fracture containment within the caprock formations. The proposed scheme is particularly designed to simulate the interactions between coupled THM processes in a CO_2 storage system (reservoir and caprock) and the propagation of a fluid-driven fracture in the so-called “leakoff-dominated” regime (Bunger et al., 2005; Garagash et al., 2011). As revealed by Fu et al. (2017), hydraulic

fracture propagation driven by CO_2 injection into a storage reservoir is expected to be in this regime, in which the majority of the injected fluid leaks from the hydraulic fracture and is stored in the storage reservoir. The propagation rate of the fracture is dominated by the leakoff rate into the reservoir. Mechanical responses of the fracture do not strongly affect the propagation rate, in sharp contrast to fracture behavior in the so-called storage-dominated and toughness-dominated regimes. This particular feature enables us to couple hydraulic fracturing and the associated rock deformation with reservoir flow in a simple yet sufficiently accurate way.

This paper proceeds as follows. Section 2 describes the mathematical formulations of a coupled THM model and the proposed modeling scheme that couples the THM model with a fracture mechanics module. The underlying rationale of this scheme is also discussed in this section. Section 3 validates the proposed scheme by comparing numerical results against the PKN solution in the leakoff-dominated regime. In Section 4 we build a 3D field-scale model, loosely based on the In Salah Project and reveal complex interplays between hydraulic fracturing and thermo-poroelastic effects induced by cold CO_2 injection. Section 5 discusses the effects of various reservoir conditions in the context of CGS, on the controlling mechanisms of the growth of caprock fracture. In the concluding section, we suggest possible implications of the proposed method and findings for GCS site characterization and operation.

2 Methodology

In this section, we briefly describe the governing equations of the coupled THM processes taking discrete hydraulic fractures into account. Next, we introduce the coupling scheme that links the coupled THM model to a fracture mechanics module in a simple yet accurate fashion. Note that the THM model used here is an extension of the continuum based THM model as described in Fu et al. (2020). More details related to that THM model, such as derivation of governing

equations of multiphase multicomponent flow and heat transfer, numerical discretization, and fixed-stress iterative scheme, can be found in Fu et al. (2020). Moreover, the detailed implementation of the fracturing module used in this study can be found in Fu et al. (2013) and Settgast et al. (2017).

2.1 Governing equations of the THM model

As presented in Fig.1, we consider a permeable body Ω bounded by the external boundary Γ that contains Dirichlet and Neumann boundary conditions for geomechanical (traction boundary Γ_t and displacement boundary Γ_u) and flow problems (prescribed pressure/temperature boundary Γ_{PT} and flux boundary Γ_F), respectively. Specifically, for the geomechanical problem, Γ is subjected to the prescribed traction $\bar{\boldsymbol{t}}$ and displacement $\bar{\boldsymbol{u}}$ applied on Γ_t and Γ_u, respectively. For the flow problem, prescribed thermodynamic conditions such as pressure $\bar{P}$, and fluxes of mass or heat ($\bar{\boldsymbol{F}}$) are applied on Γ_{PT} and Γ_F, respectively.

Domain Ω also contains an internal boundary Γ_f, where boundary conditions corresponding to a growing fluid-driven fracture in response to the injected mass q_inj are applied. Γ_f describes the fracture whose unit direction vector $\boldsymbol{n}_\mathrm{f}$ is orthogonal to Γ_f and consists of two opposing surfaces Γ_f^+ and Γ_f^- as shown in Fig.1. The body is assumed to be permeable so that leakage $\boldsymbol{F}_\mathrm{f}$ can occur from the fracture to the surrounding body through Γ_f if a positive pressure difference from the fracture to the body is present or vice versa. Note that the process of leakoff is illustrated in the enlarged inset in Fig.1.

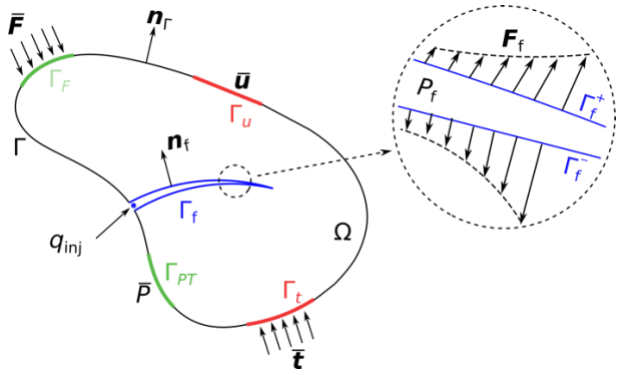

Fig. 1. Conceptual schema for modeling the evolution of a fluid-driven fracture in a permeable medium. Ω is a permeable body with an external boundary Γ that contains Dirichlet and Neumann boundary conditions for both geomechanical and flow problems. The evolving fracture in response to the injection fluid of q_{inj} is represented as an internal boundary Γ_f, highlighted in blue. The enlarged inset illustrates the leakoff of fluids $\boldsymbol{F}_f$ in the fracture through Γ_f.

The reservoir rock and the overlaying/underlying rocks (both caprock and basement) are treated as porous media subjected to fluid/heat flow as well as poromechanical deformation. The mathematical formulations and discretization strategy of the THM model are based on the following set of assumptions and treatments.

- For the fluid flow and heat transfer model, the movements of mobile phases through fractures and matrix are assumed to follow lubrication theory (Witherspoon et al., 1980) and Darcy's law, respectively.
- For the geomechanical model, the deformation of porous rock matrix is assumed to be quasi-static and linearly elastic. We use the small deformation assumption for the stress-strain relationship.
- Fractures and porous matrix are represented using separate but associated meshes: Fractures are represented with planar elements in the 3D space while the matrix is

represented with solid elements. A mapping between the two meshes is generated as the solid mesh is split to create the fracture mesh.

Additional assumptions and treatments associated with multiphase flow and heat transport model are identical to ones adopted in Fu et al. (2020).

2.1.1 Geomechanical model

The governing equations for quasi-static solid deformation of a permeable body Ω can be expressed as

$$\nabla \cdot \boldsymbol{\sigma} + \rho_{\mathrm{m}}\mathbf{g} = \mathbf{0} \tag{1}$$

where $\nabla \cdot$ is the divergence operator; $\boldsymbol{\sigma}$ is the second-order total stress tensor; $\mathbf{g}$ is the gravity vector; and $\rho_{\mathrm{m}} = \phi \sum_{J=\mathrm{A,G}} S_J \rho_J + (1-\phi)\rho_{\mathrm{s}}$ is the bulk density of matrix, in which subscript J denotes a phase of component in porous media (i.e., the aqueous (A) or gaseous (G) phase), S_J is the saturation of phase J, ρ_{s} is the grain density, and ϕ is the true porosity, defined as the ratio of the pore volume to the bulk volume in the deformed configuration (Kim et al., 2011).

Based on the thermo-poroelasticity theory (Biot 1941; Coussy 2004) and the assumptions of linearly elastic and small deformation, $\boldsymbol{\sigma}$ can be related to the temperature field and displacement field:

$$\boldsymbol{\sigma} = \boldsymbol{C}_{dr} : \nabla \boldsymbol{u} - bP_{\mathrm{E}}\mathbf{1} - 3\alpha_{\mathrm{L}}K_{\mathrm{dr}}dT\mathbf{1} \tag{2}$$

where $\boldsymbol{C}_{dr}$ is a fourth-order elastic tensor, associated with the drained-isothermal elastic moduli; ∇ is the gradient operator; $\boldsymbol{u}$ is the solid displacement vector, also the primary unknown of the geomechanical model; b is Biot's coefficient; $\mathbf{1}$ is a second-order identity tensor; α_{L} is the linear coefficient of thermal expansion; K_{dr} is the drained-isothermal bulk modulus; $P_{\mathrm{E}} = \sum_J S_J P_J - \int_{S_{\mathrm{A}}}^{1} P_{\mathrm{c}}(S)\mathrm{d}S$ is the equivalent pore pressure (Coussy 2004), in which P_J is the fluid pressure of phase J and P_{c} is the gas-water capillary pressure as a function of aqueous saturation; and $dT = T - T_{\mathrm{ref}}$ is the temperature difference, in which T is the current temperature and T_{ref} is a reference temperature.

In the geomechanical model, we consider the fluid pressure in the fracture, P_{f}, as a normal traction exerted on the fracture faces, Γ_{f}, while we neglect the shearing traction of the fluid on solid matrix. Therefore, the traction balance across the fracture surface can be written as

$$\boldsymbol{t}_{\mathrm{f}} = -P_{\mathrm{f}}\boldsymbol{n}_{\mathrm{f}} \text{ on } \Gamma_{\mathrm{f}} \tag{3}$$

The external boundary conditions, traction and kinematic, are governed by

$$\bar{\boldsymbol{t}} = \boldsymbol{\sigma}\boldsymbol{n}_t \text{ on } \Gamma_t, \tag{4}$$

$$\bar{\boldsymbol{u}} = \boldsymbol{u} \text{ on } \Gamma_u, \tag{5}$$

Where $\boldsymbol{n}_{\mathrm{f}}$ and $\boldsymbol{n}_t$ are the normal unit vectors on Γ_{f} and Γ_t, respectively; $\bar{\boldsymbol{u}}$ is the prescribed displacement on Γ_u.

2.1.2 Multiphase multicomponent flow and heat transfer model

The formulations of mass-and-energy conservation can be expressed in a unified integrodifferential form as:

$$\frac{d}{dt}\int_{\Omega_\alpha} M_\alpha^\kappa \, d\Omega_\alpha + \int_{\Gamma_\alpha} \boldsymbol{F}_\alpha^\kappa \cdot \boldsymbol{n} \, d\Gamma_\alpha = \int_{\Omega_\alpha} q_\alpha^\kappa \, d\Omega_\alpha, \quad \kappa \equiv \mathrm{c,w,\theta}; \quad \alpha \equiv \mathrm{m,f} \tag{6}$$

where subscript α denotes a type of flow model (i.e., matrix flow model when α = m, and fracture flow model when α = f); superscript κ denotes a component (i.e., CO_2 when κ = c, and water when κ = w) or heat (when κ = θ) in porous media, respectively.

For the matrix flow model (α = m), the formulation is identical to the one given by Fu et al. (2020). For the fracture flow model (α = f), the mass accumulation term M_f^κ integrating over an arbitrary volume of a fracture is given by:

$$M_\mathrm{f}^\kappa = \int_{\Gamma_\mathrm{f}} \sum_{J=\mathrm{A,G}} S_J \rho_J X_J^\kappa \, w^h \, d\Gamma_\mathrm{f} \tag{7}$$

where X_J^κ is the mass fraction of component κ in phase J and ρ_J is the density of phase J. The volume of a fracture Ω_f is assumed to be the integral of the product between its surface area Γ_f and hydraulic aperture w^h, represented by the gray volume in Fig. 2(a), which can be expressed as:

$$w^\mathrm{h} = (\boldsymbol{u}^+ - \boldsymbol{u}^-) \cdot \boldsymbol{n}_\mathrm{f} \tag{8}$$

where $\boldsymbol{u}^+ - \boldsymbol{u}^-$ is the discontinuity in the displacement field across Γ_f. Eq. (8) provides a direct coupling between the displacement field and the fracture flow.

Employing the assumption of the lubrication theory for fluid flow in fractures yields the mass fluxes term of different components, $\boldsymbol{F}_{\mathrm{f}}^{\kappa}$, expressed as

$$\boldsymbol{F}_{\mathrm{f}}^{\kappa} = -\sum_{J=\mathrm{A,G}} \rho_J X_J^{\kappa} \frac{(w^h)^2}{12\mu_J} \nabla P_J \tag{9}$$

where μ_J denotes the dynamic viscosity of fluid in phase *J*; ∇P_J is the fracture pressure gradient in phase *J*. All mass-and-heat fluxes through a fracture surface are determined via looping through its edges and summing fluxes from its neighboring surfaces. The transmissivity between fracture surfaces of different aperture is computed following the treatment given in Pruess and Tsang (1990). The mass-and-heat fluxes due to leakoff processes (as illustrated in the inset of Fig.1) can be written, using Darcy's law by assuming a Newtonian flow, as:

$$\boldsymbol{F}_{\alpha}^{\kappa} = -\sum\nolimits_{J=\mathrm{A,G}} \rho_J X_J^{\kappa} \frac{k_J^{\mathrm{r}}}{\mu_J} \boldsymbol{k}(\nabla P_J - \rho_J \mathbf{g}) \tag{10}$$

where $\boldsymbol{k}$ is the intrinsic permeability tensor of matrix elements adjacent to a fracture face. Eq. (10) shows the transmissivity of the leakoff term principally depends on the hydraulic properties of the matrix elements and the corresponding leak-off area is equal to Γ_{f}.

For the component of water in the aqueous phase, the Dirichlet (in terms of fluid pressure $\bar{P}$) and Neumann boundary conditions (in terms of mass flux $\bar{\boldsymbol{F}}$) for the coupled thermo-hydro problem can be expressed as follow:

$$\bar{F} = \boldsymbol{F}_{\alpha}^{\mathrm{w}} \boldsymbol{n}_F \text{ on } \Gamma_F, \tag{11}$$

$$\bar{P} = P_A \text{ on } \Gamma_{PT}, \tag{12}$$

where $\boldsymbol{n}_F$ is the normal unit vectors exerted onto Γ_F; Γ_F and Γ_{PT} are the fixed mass flux and fluid pressure boundaries in the matrix, respectively.

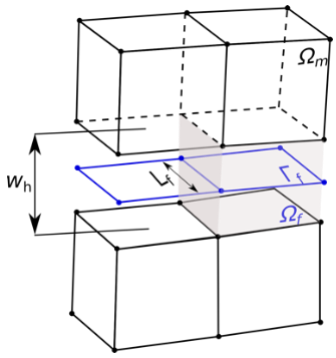

Fig. 2 Illustration of spatial discretization for coupled fracture-matrix flow model. Simulation domains of fracture are displayed in blue, matrix domains in gray.

2.1.3 Thermo-poromechanics

We employ the fixed-stress iterative scheme to solve thermo-poromechanics in rock matrix (Kim et al., 2011). In this scheme, the coupled THM problem splits into two subproblems, i.e. a fluid-heat flow problem and a geomecahnical problem. During each iteration, the subproblems are solved in an iterative sequence until the convergence of both problems. Particularly, in solving the fluid-heat flow problem, the current true porosity is estimated from its previous state with the following equation and assuming the rate of total volumetric stress remain unchanged throughout the current time step.

$$d\phi = \frac{b - \phi}{K_{\mathrm{dr}}}(dP_{\mathrm{E}} + d\boldsymbol{\sigma}_{\mathrm{v}}) + 3\alpha_{\mathrm{L}} b dT \tag{13}$$

where $\boldsymbol{\sigma}_{\mathrm{v}}$ is volumetric total stress.

The numerical treatment of implementing the fixed-stress iterative scheme follows the same procedure described in Fu et al. (2020).

2.1.4 Fracture mechanics module

We adopt the fracture mechanics module of GEOS, a high-performance computing simulation code (Fu et al. 2013; Settgast et al. 2016; Ju et al., 2020), to simulate fracture propagation. This module uses linear elastic fracture mechanics and a modified virtual crack closure technique (MVCCT) to calculate energy release rate G at the fracture tip (Huang et al., 2019). The fracture extends from the tip into intact rock when G exceeds the critical value G_c, which can be related to the critical stress intensity factor K_{IC}, also known as fracture toughness, through

$$G_c = K_{Ic}^2\left(\frac{1-v^2}{E}\right) \tag{14}$$

When fracturing occurs, new fracture faces are created by splitting the nodes between the two solid elements adjacent to the tip faces. As mentioned in the previous section, the fluid pressure along the fracture is applied to the solid elements that are connected with those faces via a normal traction force. Properly implementing this traction boundary condition is essential for satisfying the momentum balance of solid elements in the updated mesh topology. Moreover, the fluid-heat flow in newly created faces are automatically integrated into the matrix-fracture flow system, ensuring mass-and-energy balance across the entire domain.

2.2 The coupling scheme between the THM model and fracture mechanics module

The three main components of our model, (1) the multiphase multi-component solver for porous medium and fracture flow, (2) the hydraulic fracturing module, and (3) the poromechanics

294 solver, are all known to face their own numerical challenges (Kim and Moridis 2013; Settgast et
295 al., 2016; White et al., 2016). These modules are challenging even under less challenging
296 conditions, namely without the complication of fracturing for the first component and when the
297 latter two only deal with single-phase flow. In prior works, we have developed relatively robust
298 individual modules on a common platform, GEOS, for these three components (Settgast et al.,
299 2016; Fu et al., 2020). Still, coupling these three components together is a challenging task.

300 It is widely acknowledged that an implicit coupling strategy theoretically provides
301 unconditionally convergent numerical solutions and enables large timesteps for the preceding
302 coupled problem (Kim et al., 2012; Girault et al., 2016). However, the actual implementation to
303 implicitly couple the three aforementioned modules faces practically insurmountable numerical
304 difficulties, exacerbated by challenges associated with the parallel computing environment. We
305 therefore develop a sequential coupling scheme to take full advantage of existing modules in
306 GEOS. Meanwhile, as sequential coupling often suffers from poor convergence, we capitalize on
307 the inherent self-stabilizing features of leakoff-dominated fracturing to simplify the coupling
308 scheme.

309 In this scheme, we use a compositional reservoir simulator for the fluid-heat flow problem and a
310 standard Galerkin finite element method for geomechanics. As mentioned in section 2.1.4, the
311 fracture mechanics module evaluates the fracturing criterion as well as updates the solid mesh
312 and flow network once new fracture surfaces are generated. The sequential communication
313 between the THM model and fracture mechanics module is achieved by sharing key information,
314 such as fluid pressure in fractures and displacement fields, at every timestep (see Fig. 3). This
315 procedure can be performed without compromising the modularity of the code because only
316 minor modifications are required for existing individual modules.

The relationships among the physical processes involved in the problem are summarized in Table 1. Several interactions have been implicitly handled in existing modules. For instance, the fracture flow and matrix flow are solved together by unifying the fracture flow network and the matrix flow mesh in a combined flow topology as shown in Fig. 2. In other words, in the cell-centered finite volume framework, both the flow "faces" for fracture flow and the solid "elements" for matrix flow are considered "cells" interconnected together. Also, the solid deformation and matrix flow are already coupled using the "fixed-stress" scheme in the poromechanics solver. The remaining relationships are enforced sequentially as shown in Fig. 3.

As we will now explain, an inconsistency and thereby an error are introduced in the coupled solution flow. In the n^{th} iteration of each time step, the aperture is computed in Steps 3 and 4 (see Fig. 3) based on the geomechanical module's results. In iteration n+1's Step 1, the initial "guess" of the fracture cells' states is based on the solved pressure from Step 1 and the aperture from Steps 3 – 4 of iteration n. Therefore, the aperture update in iteration n would introduce a small extra (positive or negative) fluid mass to the system. We found this treatment is greatly beneficial for the convergence of the solution for the following reason. An open fracture's aperture is extremely sensitive to fluid pressure. If we use the fluid mass in each fracture cell from iteration n's Step 1 while using the updated aperture, the initial "guess" of the flow system's state in iteration n+1 would be highly volatile and usually far from the "true" solution, resulting in severe convergence difficulties. We hypothesize that the fluid mass inconsistency is inconsequential for the overall accuracy of the solved system because only a very small fraction of the injection fluid is stored in the fracture, a salient feature of the leakoff-dominated regime. In the verification solution in Section 3 and simulation results in Section 4, we compare the total masses of CO_2 in the numerical models with the total injected quantities to quantify the induced

error. Note that rock porosity is not very sensitive to pressure change, so this treatment is unnecessary for the rock matrix cells.

Table 1. Coupling relationships between individual modules. The "step" in each cell refers to an "operation" in the flow diagram in Fig. 3 where the interaction is embodied.

Modules providing information	Modules receiving information			
	Fracture Flow	Matrix flow	Solid deformation	Fracture mechanics
Fracture Flow	Self	Pressure boundary condition along fracture faces; solved together.	Traction boundary condition along fracture faces. Step 2.	Indirect influence, through solid deformation
Matrix flow	Fluid leakoff; solved together	Self	Solved together in poromechanics	Indirect influence, through solid deformation
Solid deformation	Hydraulic aperture and fluid storage. Step 4.	Solved together in poromechanics	Self	Compute energy release rate. Step 0.
Fracture mechanics	New fracture flow elements. Step 0.	Indirect influence, through fracture flow	Updated mesh. Step 0.	Self

We found the sequential coupling scheme to have satisfactory numerical performance: Most time steps converge within five iterations; The scheme is stable provided the time step is significantly smaller than the time that it takes the fracture to propagate the distance of one-element length.

This is again largely owing to the self-stabilizing features of fracture propagation in the leakoff-dominated regime: As the permeability of the reservoir is largely constant, the leakoff rate is mostly determined by the difference between fluid pressure in the fracture and the far-field fluid pressure in the reservoir. In a propagating fracture, the fluid pressure is always marginally higher than the "fracture propagation pressure", which, in the scenarios concerned by this study, is approximately the "fracture opening pressure" near the fracture front. The fracture opening pressure is in turn determined by the total stress in the system, which evolves very slowly. Therefore, a convergent numerical solution can be obtained as long as the effects of the extending fracture surface area on the flow into the rock matrix are captured.

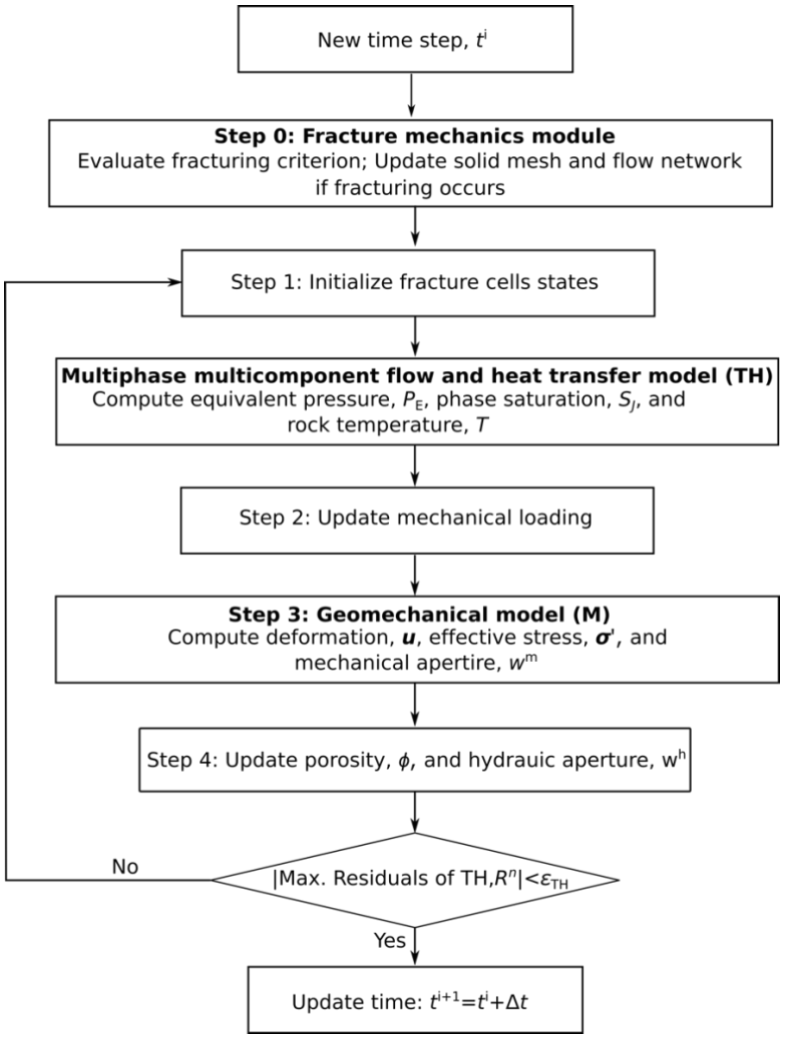

Fig. 3. Flowchart of the coupling scheme between coupled THM coupled model and fracture mechanics module. The coupling convergence criterion of coupled THM model is that the maximum residuals of TH model is smaller than ε, a pre-set small value, say 10^{-5}, after updating perturbed hydraulic variables.

3 Verification

In this section, we compare the new model's results with the PKN solution in the leakoff-dominated regime to verify the numerical implementation of the model and, particularly, to validate the coupling scheme presented in Section 2.2.2. Note that the validation of relevant individual submodules in GEOS has been reported in previous works, in which numerical results are compared with the analytical solutions of poromechanics (Terzaghi's and Mandel's problems (Fu et al., 2019; Fu et al., 2020)), and of fracturing propagation in different regimes (Fu et al., 2013; Settgast et al., 2017).

3.1 The PKN solution in the leakoff-dominated regime

We use a standard fracture geometry, the PKN model as illustrated in Fig. 4(a), to test the proposed coupling scheme (Perkins and Kern 1961; Nordgren 1972). The origin of the coordinate system is set at the injection point; the *x*-direction coincides with the fracture propagation direction, so the y-axis is along the direction of the minimum principal *in situ* stress S_{hmin}. Recall that hydraulic fracturing in a storage reservoir with moderate permeability is in the leakoff-dominated regime. We therefore compare the numerical solutions against the PKN model in the so-called leakoff-dominated regime (Nordgren 1972). This solution describes the growth of a fixed-height vertical fracture when the volume of fluid loss into the reservoir is much larger than the volume stored in the fracture.

According to the analytical solution (Nordgren 1972), the half fracture length L_f and aperture w_0^h at the wellbore are

$$L_f = \frac{qt^{1/2}}{2\pi C_L h_f} \tag{15}$$

$$w_0^h = 4\left[\frac{\mu q^2}{\pi^3 E' C_L h_f}\right]^{\frac{1}{4}} t^{1/8} \tag{16}$$

where q is the total injection rate; h_f is the fracture height; $E' = E/(1-\nu^2)$ is the plane-strain modulus for the formation; and C_L is the Carter's leakoff coefficient. As revealed in Howard and Fast (1957), C_L can be expressed as:

$$C_L = \Delta P\left(\frac{k_r \phi c_t}{\pi \mu}\right)^{1/2} \tag{17}$$

where ΔP is the difference between the fracture pressure and the remote reservoir pressure that is assumed to be constant; k_r is the intrinsic permeability of the reservoir; and $c_t = c_f + c_p$ is the total compressibility, where c_f is fluid compressibility and c_p is pore compressibility, both of which are constants in equation (17). However, in a high-fidelity numerical model, c_f and c_p respectively depend on the nonlinear PVT properties of fluids and the solid deformation in the coupled THM models. Therefore, when applying the analytical solution, we set c_t to the value computed from the numerical models for simplicity. Also note that equation (17) assumes 1D diffusion, which is not necessarily valid in a real reservoir or in a high-fidelity numerical model.

Some additional, special adaptations of the numerical model are needed to be consistent with assumptions of the analytical solution. The analytical solution intrinsically assumes zero toughness for the reservoir rock. Accordingly, we set the toughness of reservoir rock to 100 Pa•m$^{0.5}$, a small finite value that prevents small numerical noise from triggering fracturing artificially. The analytical solution calculates leakoff using Carter's leakoff coefficient, which is based on 1D diffusion. However, the fluid flow in the THM coupled model is 3D in nature. To match the 1D diffusion assumption, we use a strongly anisotropic permeability (k_{ry}=10 mD, k_{rx}=k_{rz}=0 mD). We also run an additional simulation by removing the 1D diffusion restriction for comparison. Moreover, the Biot coefficient is set to zero in the numerical model, since the PKN model does not incorporate the poromechanical effects in the reservoir. Note that none of the above adaptations is used in the 3D simulations in section 4 and beyond.

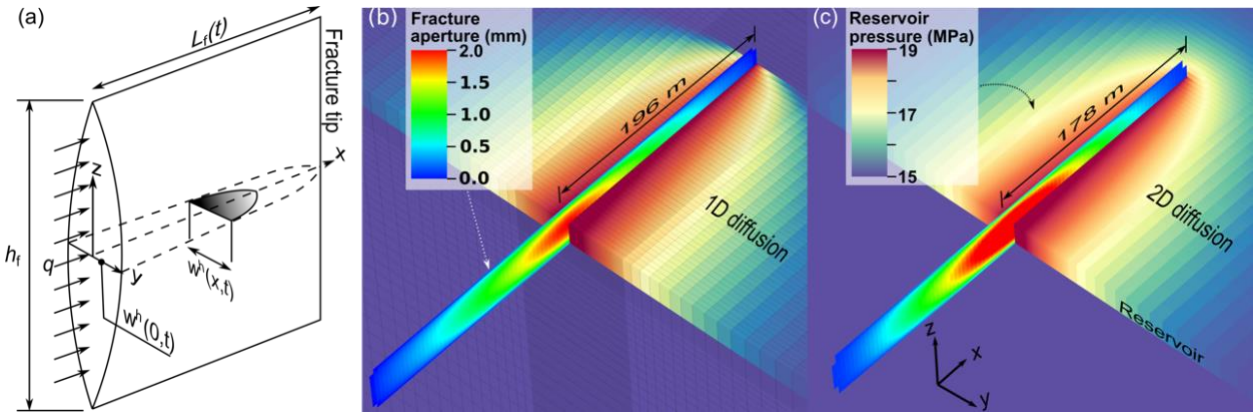

Fig. 4. Geometrical characteristics (a) and simulation results for a PKN fracture with q=0.04 m^3/s in the case of (b) 1D diffusion and (c) 2D diffusion at t=4×10^{5}s. In (a) where only one wing of the fracture is shown due to symmetry, h_f, q, w^h, and L_f indicate fracture height, injection rate, fracture width (aperture), and fracture length, respectively. In (b) and (c), a full length/height of the fracture and a quarter of the reservoir pressure field are presented. Note that fracture color scale indicates fracture aperture, whereas the color scale for the matrix indicates reservoir pressure.

3.2 Numerical realization of the PKN model

The numerical simulation only models one quarter of the problem owing to the symmetrical condition of PKN model, as shown in Fig. 4(a). To minimize boundary effects, the dimensions of the quarter model are 1000 m, 2000 m, and 1000 m in *x*-, *y*-, and *z*-directions, respectively, where meshing in each dimension contains a refined portion (200 m, 100 m, and 40 m in *x*-, *y*-, and *z*-directions, respectively) and coarse portion. The refined region uses constant mesh resolutions in three directions, i.e. 4 m, 1 m, and 2 m, respectively, whereas the coarse region uses a progressively coarser mesh resolution toward the far-field. The model is discretized into 1,004,731 hexagonal elements. We simulate fracture propagation and reservoir response for three different injection rates as listed in Table 1. The fourth simulation removes the 1D diffusion restriction for the baseline injection rate and results are denoted by "2D diffusion" in Fig. 4 and 5. Parameters adopted in the verification are listed in Table 1.

Table 1. Parameters employed in the numerical model for the simulation of the PKN model.

Property	Value
Fracture height, H_f	40 m
Injection rate, q	0.02, 0.04[a], and 0.06 m^3/s
Dynamic viscosity, fluid, μ	1×10^{-3} Pa s
Porosity, ϕ	0.2
Pore compressibility, c_t	1.04×10^{-8} Pa^{-1}
Poisson's ratio, v	0.25
Biot's coefficient, b	0.0
Carter's leakoff coefficient, C_L	0.493 mm/$\sqrt{s}$
Young's modulus, E	10 GPa
Critical stress intensity factor (toughness), reservoir	100.0 Pa•$m^{0.5}$

[a]baseline case simulation

3.3 Verification results

Fig. 5 shows a comparison of results from the numerical simulation and the PKN solutions. In general, the temporal evolution of fracture length for the three injection rates are in good agreement with the corresponding analytical solutions. The numerically simulated apertures tend to deviate from the analytical solutions early in the injection but gradually converge to the solutions as injection progresses.

The disparity between the numerical solution and the PKN solution at the early times is likely caused by the geometric assumptions of the PKN model, i.e. the fracture length being much larger than the fixed fracture height (a rectangular fracture shape). In the early stage of injection, the fracture length simulated by the numerical model, however, is smaller than or similar to the preset fracture height, forming a penny shape and therefore a direct comparison between solutions with different fracture shape assumptions is not appropriate. Note that for all the three injection rates, the numerically predicted apertures become very similar to the analytical solutions when the half fracture length in each case reaches around 200 m, 2.5 times the fracture height. Fig. 5(b) also shows that numerical results of wellbore aperture exhibit a moderate oscillatory behavior. This behavior is expected because the spatial discretization scheme dictates that the fracture has to propagate by the length of an element, yielding numerical overshoot/undershoot.

As shown in Fig. 5(c), the percentage of fluid in the fracture compared with the total injection volume, termed "*fracture volume ratio*" in this study, is quite low, generally less than 1%. This confirms that these four simulated hydraulic fractures are indeed in the leakoff-dominated regime. Note that the "fracture volume ratio" is mathematically identical to the "fluid efficiency"

used in unconventional reservoir stimulation. However, we avoid using this established term because in carbon storage, retaining more fluid in the fracture, i.e. achieving a “high fluid efficiency”, is not an objective.

Fig. 5(d) shows the temporal evolution of “*mass loss ratio*”, defined as the percentage of mass loss induced by the coupling scheme compared with total injection mass in this study. Note that a negative mass loss ratio means extra masses are introduced in the system. A small yet noticeable error is introduced at early time by the inconsistency in the coupling scheme. However, this inconsistency rapidly diminishes, and the absolute mass losses converge to near 0.05 % as the leakoff dominates. The convergence of mass loss ratio for each case validates our hypothesis that the mass loss induced during the coupling is indeed trivial and proves the accuracy of our coupling scheme for simulating leakoff-dominated fracturing.

The comparison between Fig. 4(b) and (c) shows the fracture length grows faster in the case of 1D diffusion than that of 2D diffusion where the reservoir pressure plume front goes farther than the crack tip. Likewise, Fig.5 (a) and (c) shows that the case of 2D diffusion yields a slightly higher leakoff compared with the baseline verification (1D diffusion), which includes lower fracture growth rate and smaller wellbore aperture. Those behaviors are mainly owing to the overestimation of the actual C_L when 2D diffusion is invoked (Carrier and Grant, 2010; Fu et al., 2017).

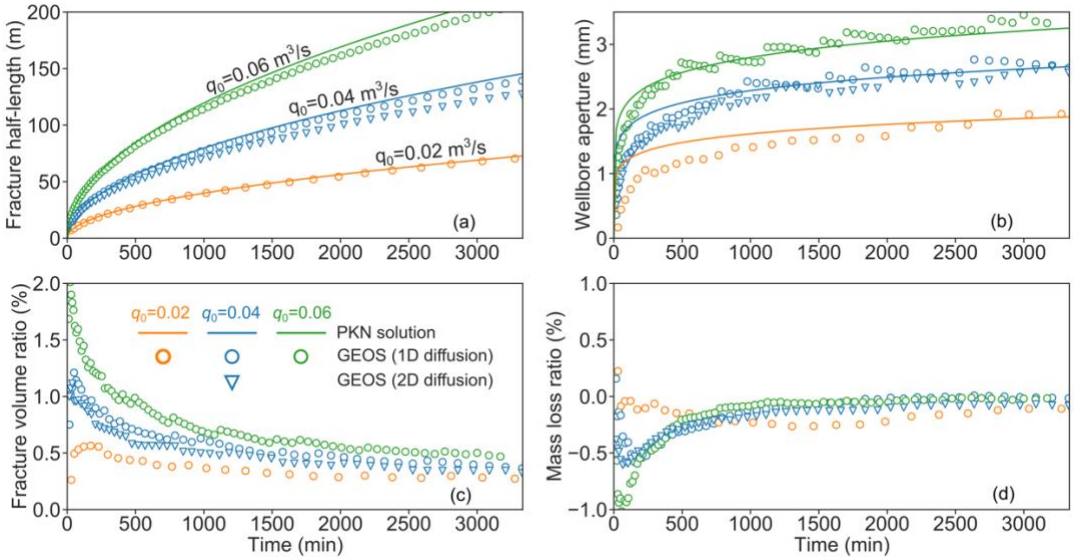

Fig. 5. Simulation results for a PKN fracture in the leakoff-dominated regime. (a), (b), (c) and (d) plot the temporal variations of fracture half-length, wellbore aperture, fracture volume ratio, and mass loss ratio respectively. Analytical solutions for leakoff-dominated fractures are plotted in (a) and (b) for comparison. The fracture volume ratio in (c) denotes the percentage of the total injected fluid stored in the fracture. The mass loss ratio in (d) denotes the percentage of the mass loss induced by the coupling scheme compared with the total injection mass.

4 Application in simulating fracturing into caprock

To demonstrate the capabilities of the proposed scheme and apply it to GCS, we build and analyze a field-scale 3D numerical model (hereafter referred to as the baseline case) in GEOS in this section. The baseline model is loosely based on the geological settings of the In Salah storage site (Rutqvist et al., 2010; Ringrose et al., 2013; White et al., 2014), as shown in Fig. 6 (a), while the analyses generally apply to a GCS reservoir with marginal permeability.

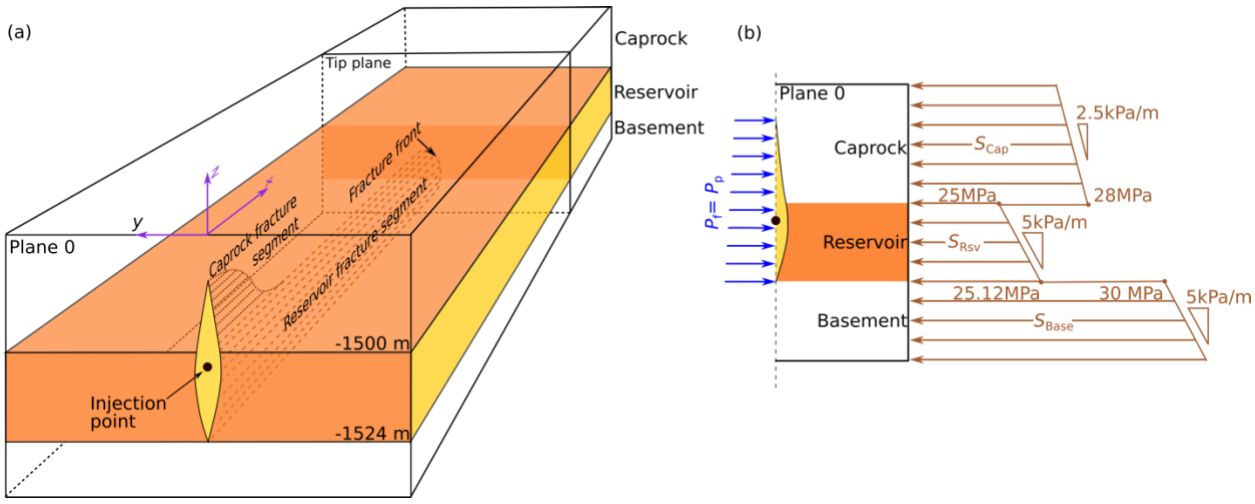

Fig. 6. (a) 3D schematic (not to scale) of the configuration, geometry and dimensions of the baseline model showing one wing of a hydraulic fracture penetrating into the caprock, with cold supercritical CO_2 entering the computational domain from the injection point, marked as a black dot on the plane 0 (x=0). Tip plane tracks the movement of fracture front. Sub-figure (b) shows internal and external traction boundary conditions, i.e. fracture pressure and horizontal *in-situ* stress, applied to the 3D model on plane 0. Note that only one wing of the fracture in panel (a) is shown due to symmetry.

4.1 Model setup

Fig. 6(a) schematically depicts the 3D geometry of the baseline model. The CO_2 storage reservoir of marginal permeability is sandwiched between the caprock and the basement, both of which are much less permeable. The reservoir is 24 m thick with its interface with the caprock located at 1500 m depth (z = -1500 m). We established a 3D coordinate system, in which the *x*-axis is parallel to the direction of the maximum *in situ* horizontal stress (S_{Hmax}), the *y*-axis is parallel to the direction of minimum *in situ* horizontal stress (S_{hmin}), the *z*-axis points upward, and the origin at ground surface resides above the injection point. The injection point is annotated as a black dot in Fig.6 (a) to highlight its position. Note that the vertical location of the injection point should not alter the outcome of fracturing because there is no fracturing barrier

inside the reservoir. The initial pore pressure follows the hydrostatic distribution and the initial reservoir temperature is set as 65 °C. The minimum principal *in situ* stress (S_{hmin}) follows a segmented-linear distribution along the *z* direction, as shown in the right portion of Fig. 6(b). S_{hmin} spatial distributions with caprock, reservoir, and basement layers are denotated by S_{Cap}, S_{Rsv}, and S_{Base}, respectively. We assume that there is a fracturing barrier between the reservoir and basement that prevents downward fracturing as we mainly focus on conditions and mechanisms for fracturing in the reservoir and caprock. As illustrated in Fig. 6(a), the fracture propagation is assumed to only take place within the *x*-*z* plane, perpendicular to the direction of S_{hmin}. Note that the symmetry of the system with respect to the *y*-*z* plane at the injection point allows the use of a half model.

Fully-saturated supercritical CO_2 at an injection temperature of 45°C, is injected into the reservoir at a constant rate of 15.0 kg/s (one wing of fracture), approximately a million metric ton per year. We assume that the injection well is cased, and fractures are initiated from perforations, which limits the well only to communicate with the system through the fracture. Thus, the injection well can be simplified as a point source in our 3D computational domain. The so-called “roller” boundary condition is applied to all “far-field” boundaries of the geomechanical model. For the fluid flow model, prescribed mass/heat rate conditions for the injection well are applied at x= 0, y=0 and z=-1504 m. We apply the original reservoir pressure and a constant ambient temperature (65°C) at the lateral boundaries as the far-field Dirichlet boundary conditions. No-flow conditions are applied to elements on the top and bottom planes.

The computational domain of the baseline case has a core region whose dimensions in *x*-, *y*-, and *z*-directions are 800 m, 200 m, and 240 m, respectively. The core region has a relatively fine mesh resolution of 8.0, 4.0, and 8.0 m in those directions. Surrounding the core region is a

coarsely resolved region that extends to 5800 m, ±9000 m, and ±400 m in the respect three directions, which mitigates boundary effects while maintaining computational efficiency. The baseline model involving a kilometer-scale reservoir and 3 years of injection time, is discretized into 1,344,000 elements and the simulation is conducted across 252 CPU cores (16 Intel® Xeon® E5-2670 CPUs), which runs for 18 hours on a high-performance computer (4536 core-hours in total).

Table 3 summarizes the computational parameters and constitutive models for the baseline model. As for the mobility-related constitutive models in multiphase flow model, we use a Corey-type relative permeability functions (Brooks and Corey, 1964) and a van Genuchten capillary function (Van Genuchten, 1980), respectively written as Eq. (18) and (19).

$$k_{\mathrm{A}}^{\mathrm{r}} = S_{\mathrm{n}}^{4},\ k_{\mathrm{G}}^{\mathrm{r}} = (1 - S_{\mathrm{n}})^{2}(1 - S_{\mathrm{n}}^{2}) \qquad (18)$$

$$P_{\mathrm{C}} = -P_0[(S^*)^{-1/\lambda} - 1]^{-1/\lambda},\ S^* = (S_{\mathrm{A}} - S_{\mathrm{irA}})/(1.0 - S_{\mathrm{irA}}) \qquad (19)$$

where $k_{\mathrm{A}}^{\mathrm{r}}$ and $k_{\mathrm{G}}^{\mathrm{r}}$ are relative permeabilities in aqueous and gaseous phases; $S_{\mathrm{n}} = (S_{\mathrm{A}} - S_{\mathrm{irA}})/(1.0 - S_{\mathrm{irA}} - S_{\mathrm{irG}})$ is the normalized aqueous saturation; S_{irA} and S_{irG} are the irreducible aqueous saturations and the residual gas saturations, respectively. λ and P_0 are the exponent that characterizes the capillary pressure curve and the capillary modulus, respectively. Then, we set S_{irA} = 0.12 and S_{irG} = 0.01 for relative permeability, and S_{irA} = 0.11, P_0= 12500 Pa, and λ = 0.254 for capillarity, where the capillary pressure model employs a slightly smaller S_{irA} than the model of relative permeability in order to prevent unphysical behavior (Moridis and Freeman, 2014).

Table 2. Parameters employed in the baseline simulation

Property	Baseline value
Reservoir thickness, H_r	24 m
Minimum principal *in situ* stress in reservoir, total stress, mid-depth, S_{hmin}^{r}	25 MPa
Minimum principal *in situ* stress in caprock, total stress, mid-depth, S_{hmin}^{c}	30 MPa
Initial pore pressure, mid-depth of reservoir, P_{int} (hydrostatic condition applies)	15 MPa
Biot's coefficient, reservoir rock, b_r	0.5
Biot's coefficient, caprock, b_c	0.25
Intrinsic permeability, reservoir, k_r	15 mD
Intrinsic permeability, other layers, k_c	0.1 μD
Porosity, reservoir, ϕ_r	0.15
Porosity, all other layers, ϕ_c	0.05
Young's modulus, all layers, E	10 GPa
Poisson's ratio, all layers (Armitage et al., 2010), v	0.25
Initial temperature, all layers, T_{Int}	65 °C
Coefficient of thermal expansion, linear, α_L	10^{-5} /°C
Injection temperature, T_{Inj}	40 °C
Thermal conductivity, all layers, λ	3.0 W/(m·K)
Heat capacity, all layers, C_s	1000 J/(kg·K)
Critical stress intensity factor (toughness), all layers (Senseny and Pfeifle, 1984)	1.0 MPa·$m^{0.5}$
Relative permeability model[a] (Brooks and Corey, 1964)	$k_A^r = S_n^4$ $k_G^r = (1 - S_n)^2(1 - S_n^2)$ $S_n = (S_A - S_{irA})/(1.0 - S_{irA} - S_{irG})$ S_{irA} = 0.12, S_{irG} = 0.01

Capillary pressure model[b] (Van Genuchten, 1980)	$P_C = -P_0[(S^*)^{-1/\lambda} - 1]^{-1/\lambda}$ $S^* = (S_A - S_{irA})/(1.0 - S_{irA})$ S_{irA} = 0.11, P_0 = 12500 Pa, λ = 0.254

a k_A^r and k_G^r are relative permeabilities in aqueous and gaseous phases; S_n is the normalized aqueous saturation; S_{irA} and S_{irG} are the irreducible aqueous saturation and the residual gas saturation, respectively

b P_0 is the capillary modulus

4.2 Results of baseline model

As presented in Fig. 7 and Fig. 8, results of the baseline model clearly show how a leakoff-dominated fracture is driven by injection and provides an evolving interface between injection and reservoir storage. By the end of three years of injection, the fracture has propagated 620 m into the reservoir, providing a growing interface plane for feeding injected CO_2 into the reservoir. The CO_2 plume advances approximately 625 m in the *y*-direction on each side (Fig. 8(p)), spanning an area of reservoir as large as about 1.24×1.25 kilometers. Note that the rate of injection employed in the baseline case cannot possibly be achieved if the downhole injection pressure is strictly limited to below the estimated fracturing pressure of the caprock, approximately 25 MPa. Meanwhile, the maximum fracture height only reaches 88 m, thereby being vertically contained in the lower portion of the caprock (Fig. 7(b) and Fig. 8(m)). Note that the containment mechanism will be elucidated in the subsequent analysis.

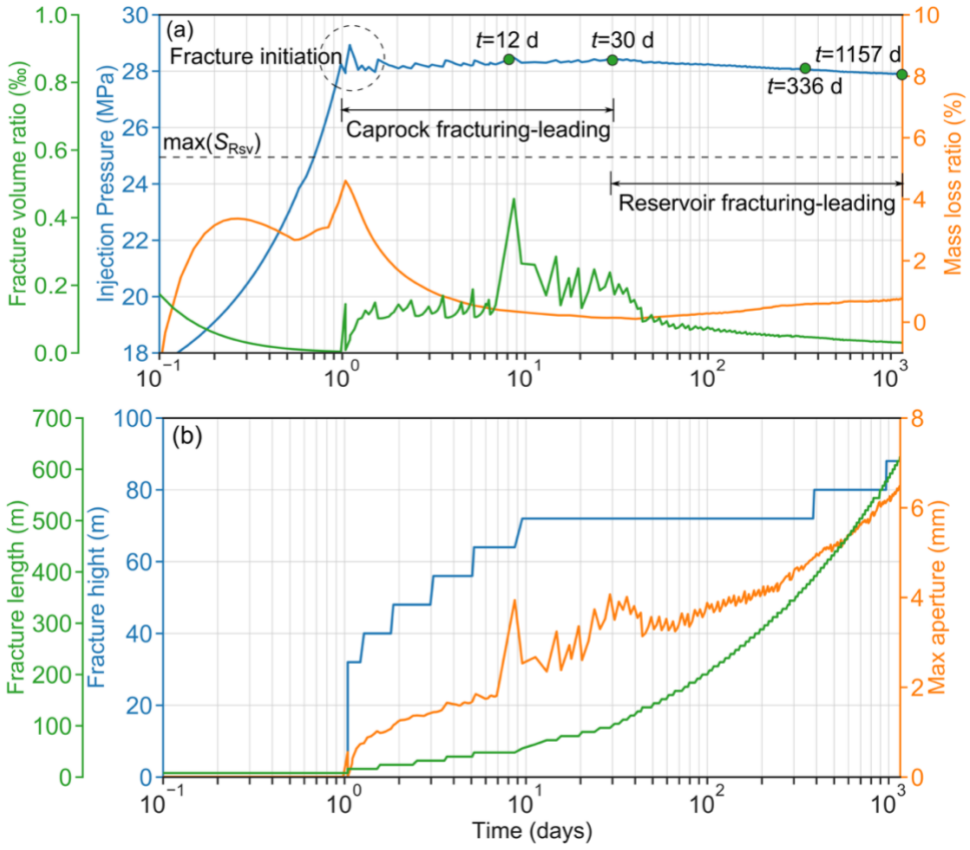

Fig. 7. Overall responses of the system in the baseline case. (a) Fracture volume ratio, injection pressure, and mass loss ratio versus time; (b) Fracture length, fracture height, and max aperture versus time. The curve colors in (a) and (b) correspond to their *y* axes. Fracture volume ratio is the percentage of injected fluid retained in the fracture. Injection pressure is measured at the injection point at the entrance to the fracture. Mass loss ratio is the percentage of injected CO_2 mass that is "lost" due to the error introduced by the sequential iteration scheme as explained in section 3.3. Note that the highest stress level of S_{Rsv}, max(S_{Rsv}), which is the in situ stress magnitude at the bottom of the reservoir, is indicated by a black dash line in (a).

Another interesting observation is the evolution of injection pressure (the blue line in Fig. 7(a)) at the entrance to the fracture over time, which can be divided into three stages: (1) the initially rapid pressure buildup before apparent fracture growth (about 1 day), (2) the pressure plateau as fracture propagates (from 1 day to 30 days), and (3) the subsequent slow pressure decline (after 30 days). In the first stage, accommodating the injection rate requires sustaining an open fracture

in the reservoir, which in turn requires a continuously increasing injection pressure, much higher than original S_{Rsv}, owing to the effect of back-stresses caused by pressure diffusion into the reservoir (Detourney and Cheng, 1997; Kovalyshen, 2010). Fu et al. (2020) had modeled how this effect causes rapid increase of injection pressure and eventually causes fracturing of the caprock.

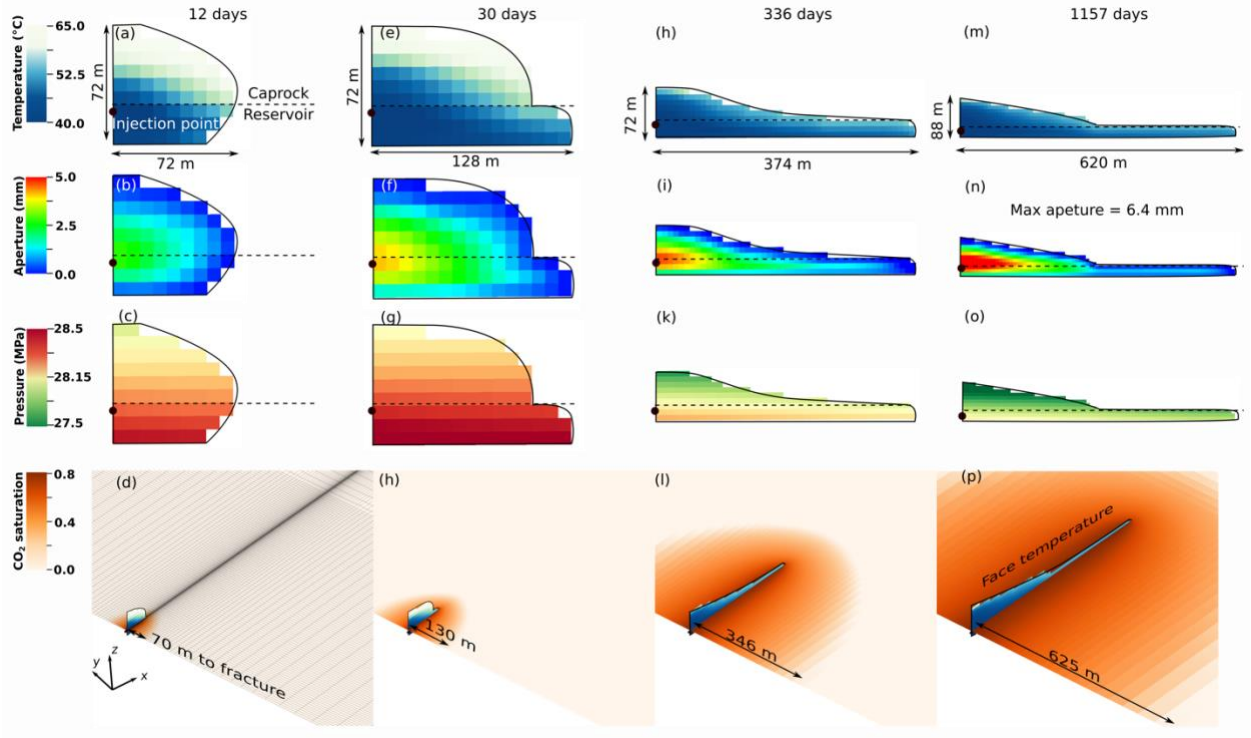

Fig. 8. Four selected states of the hydraulic fracture and the reservoir rock. The first three rows present snapshots of temperature (first row), aperture (second row), and pressure (third row) on the evolving hydraulic fracture. The last row shows the spatial-and-temporal evolution of CO_2 (critical state gas phase) in the reservoir (z=-1510 m). The interface between the reservoir and the caprock is denoted by a dark dashed line and the injection point is annotated as a black dot. Note that scales vary among the columns of the first three rows for clearer visualization, whereas the four sub-figures in the fourth row use the same scale.

Here we mainly focus on the evolution of fracture propagation after caprock fracturing takes place, which spans the second and third stages as designated in this section. Fig. 8 shows four

representative states of the fluid-driven fracture and CO_2 saturation (supercritical state gas phase) in the reservoir rock, at 12 days (in second stage), 30 days (transition from second to third stage), 336 days and 1157 days (both in third stage). In the second stage when the pressure is largely constant, fracturing in caprock seems to lead fracturing in the storage reservoir. The constant injection pressure in this stage reflects the fracturing pressure of the caprock, which is mainly influenced by S_{Cap}. Note that the injection pressure is only slightly higher than S_{Cap} near the reservoir-caprock interface. In the third stage, reservoir fracturing leads the fracture length growth and the injection pressure slowly declines as explained in Section 4.2.2. This pattern change suggests an evolution of fundamental physical mechanisms that dominate fracture growth as elucidated in the subsequent sections.

4.2.1 Second stage: caprock fracturing-leading

Fig. 9 presents spatial distributions of the fluid pressure, temperature, effective stress, and total stress in two vertical cross-sections (near the injection and near the fracture tip, respectively) and two horizontal cross-sections (in the reservoir rock 10 m below the bottom of the caprock, and in the caprock 30 m above the top of the reservoir rock) after 12 days of injection. Pore pressure propagates in the reservoir much farther than in the caprock, due to the much higher permeability of the reservoir (150,000 times higher than that of the caprock). Significant temperature decreases only take place within a short distance from the fracture in the reservoir (Fig. 9 (e) and (f)), while temperature change in caprock is hardly perceptible (Fig. 9 (g)). Although thermo-mechanical effect tends to reduce the total stress in the cooled region in the reservoir, the effect of poroelasticity on increasing the total stress in this case is much stronger. As a result, the total stress near the fracture in the reservoir even becomes higher than in the caprock, although initial

615 S_{hmin} in the reservoir was on average 3 MPa lower than that of the caprock. This reversed stress
616 contrast tends to hamper fracture propagation in the reservoir, favoring easier propagation in the
617 caprock.

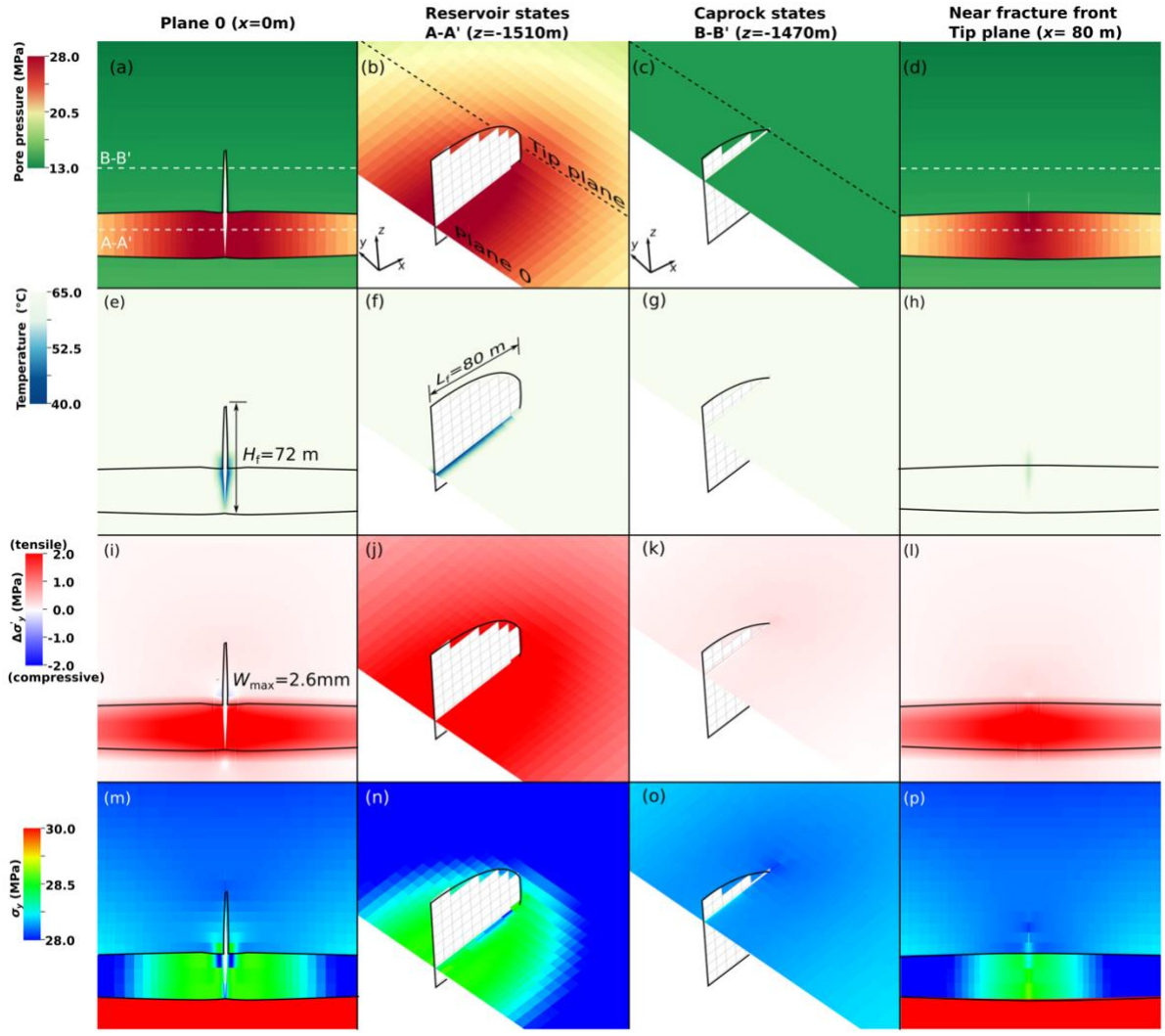

618

619 Fig. 9. States of the reservoir rock and the caprock after 12 days of injection. The four rows of panels show spatial
620 distributions of pore pressure (first row), temperature (second row), effective stress increment (third row), and
621 horizontal total stress (fourth row). The first and fourth columns respectively show the distributions of variables on
622 two vertical planes cutting the injection point and the fracture tip, respectively. The second and third columns show
623 the distributions of the variables on two horizontal planes A-A′ (reservoir) and B-B′ (caprock) respectively. The
624 deformation of first and fourth columns is magnified by 500 times.

4.2.2 Third stage: reservoir fracture-leading stage

The system response in this stage is depicted using spatial distributions of the same variables as used in the preceding section but for a much later state, 1157 days into the injection (Fig. 10). In general, the most marked difference from the second stage is that the fracture has horizontally grown much longer, which mostly takes place in the reservoir rock, and that the cooling front in the reservoir has advanced much farther (i.e. thermal penetration depth is comparable to fracture height).

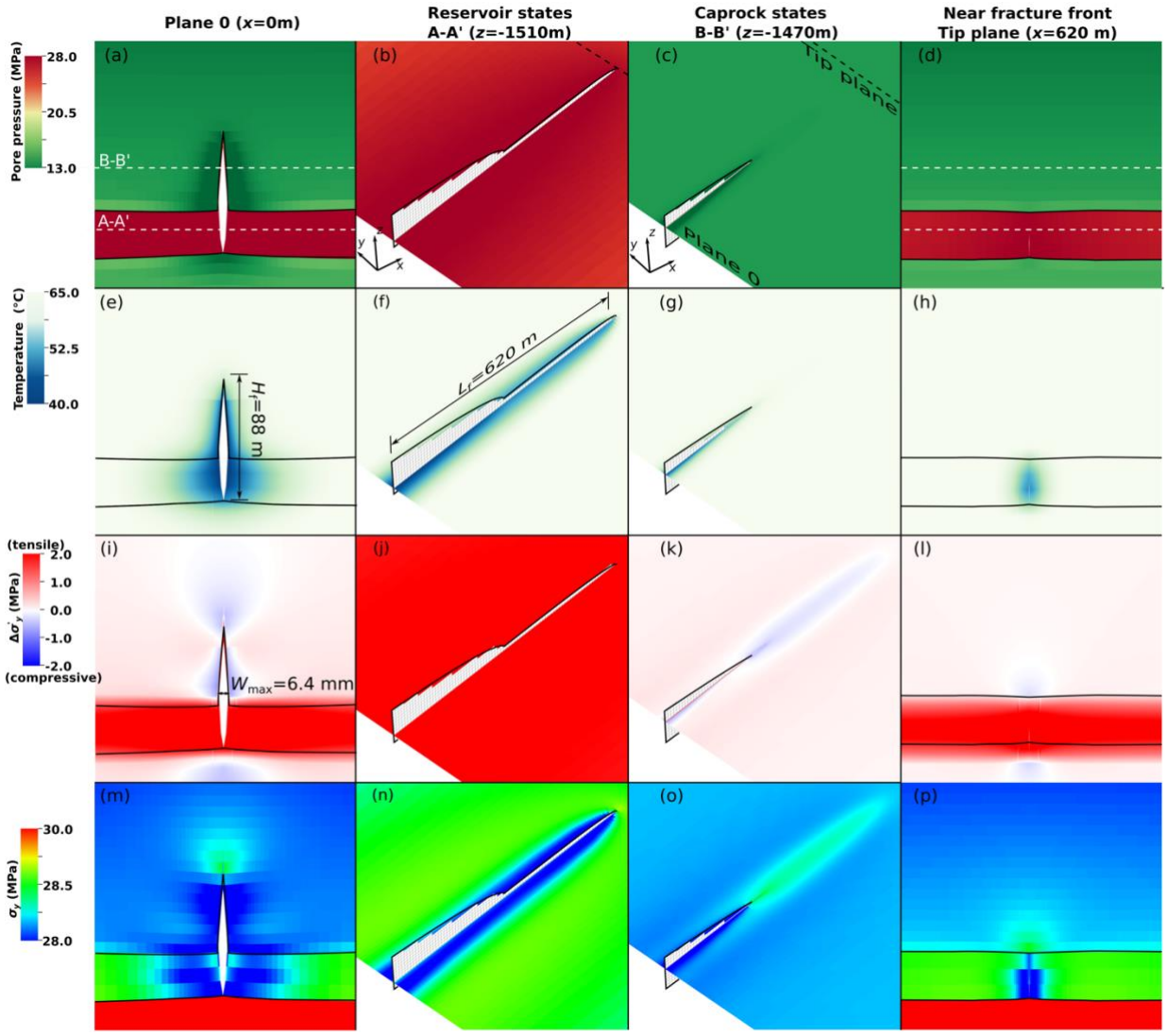

Fig. 10. States of the reservoir rock and the caprock after 1157 days of injection. The four rows of panels show spatial distributions of four variables, namely pore pressure ((a) through (c)), temperature ((d) through (f)), effective stress increment ((g) through (i)), and horizontal total stress ((j) through (i)). The first and fourth columns respectively show the distributions of variables on two vertical planes cutting the injection point and the fracture tip, respectively. The second and third columns show the distributions of the variables on two horizontal planes A-A′ (reservoir) and B-B′ (caprock) respectively. The deformation of first and fourth columns is magnified by 500 times.

Unlike the rapid and continuous horizontal propagation, the vertical propagation is slow and contained, since only an absolute height growth of 16 m takes place throughout this stage (Fig. 10 (e) and Fig. 7 (b)). This vertical containment of the fracture is mainly because of a favorable stress gradient. The adopted gradient of S_{hmin} such that $-\mathrm{d}S_{\mathrm{hmin}}/\mathrm{d}z < \rho_{\mathrm{c}}g$ provides a relatively stable condition that halts the upward propagation. This is because it takes more hydraulic head for the caprock fracture to grow at a higher position (Fu et al. 2017).

Fig. 10(e) shows the cooling front in the reservoir rock has advanced a distance equal to approximately half of the fracture height, nearly 40 m. This results in a significant decrease of total stress perpendicular to the fracture, despite the poromechanical effect that tends to increase the total stress (Fig. 10(n)). Meanwhile, the total stress of regions near the fracture front in the caprock is not reduced by the thermo-mechanical effect but rather slightly increases (fig. 10(o)). This stress increase is mostly owing to the additional compression of the caprock to compensate for the cooling contraction of the reservoir. Other studies have also reported this compression of the caprock induced by the injection of cold CO_2 into the reservoir (e.g. Vilarrasa and Laloui, 2015; Salimmda et al. 2017). In this state, the cooling of the reservoir tends to have opposite effects on the total stresses of the reservoir and the caprock. Therefore, the net effect of this discrepancy is that it is much easier to fracture the reservoir rock than the caprock.

Another key observation in this stage is a gradually decreasing injection pressure (Fig. 7(a)). This pressure decrease is owing to the effect of cooling on the total stress of the fracture tip region. In the second stage, the fracture tip region, located in the caprock, is largely unaffected by the cooling front (Fig. 9(g)). In this stage, however, the cooling front has traversed the fracture entirely and the near tip region has been cooled, which results in a decrease of total stress (Fig. 10(h) and (p)) and therefore the fracturing pressure decreases.

Note that in all stages analyzed, the propagation of the fracture is still in the leak-off dominated regime and the mass loss introduced by the coupling scheme is marginal, as clearly shown in Fig.8(a). These results demonstrate that the proposed modeling scheme can be employed to effectively simulate fracture propagation in a leakoff-dominated regime without compromising its accuracy.

5 Effects of the magnitude of *in situ* stresses in the caprock

As reflected in the baseline simulation, the caprock *in situ* stress S_{Cap} plays significant roles in determining the evolution of pumping pressure and affecting the pattern of fracture propagation. However, to what extent the stress difference between S_{Cap} and S_{Rsv} affects the fracture propagation and containment is still unclear. In this section, we evaluate the effects of S_{Cap} on the growth and vertical containment of fluid-driven fractures. Note that $\bar{S}^{\mathrm{C}}_{\mathrm{hmin}}$ presented in this section denotes the greatest horizontal minimum stresses in the caprock, which is the stress level at the interface with the reservoir.

Fig. 11 show the effects of $\bar{S}^{\mathrm{C}}_{\mathrm{hmin}}$ (varying from 26 MPa to 32 MPa) on fracture propagation and fracture geometries (i.e. fracture heights and lengths). A lower $\bar{S}^{\mathrm{C}}_{\mathrm{hmin}}$ is expected to reduce vertical containment of caprock fracturing. Especially in the case with $\bar{S}^{\mathrm{C}}_{\mathrm{hmin}}$= 26 MPa, the

maximum fracture height reaches around 192 m, far exceeding the thickness of the reservoir (i.e., 24 m). However, the fracture heights (i.e., 32 and 40 m) in cases with $\bar{S}^{C}_{hmin}$= 30 and 32 MPa are both slightly larger than 24 m and the fracture height (i.e., 88 m) in the baseline lies in between. Meanwhile, the case with $\bar{S}^{C}_{hmin}$=26MPa where caprock fracturing leads the fracture growth throughout the entire simulation has a long fracture length (i.e. 1053 m after 3 year of CO_2 injection (Fig. 11(a))), whereas the rest of the cases ($\bar{S}^{C}_{hmin}$=28MPa, 30MPa, and 32 MPa) have shorter fracture lengths that are similar to each other (i.e. around 650 m at the end of the simulation (Fig. 11(b), (c) and (d))). This discrepancy is caused by the significantly lower leakoff coefficient for the case with $\bar{S}^{C}_{hmin}$=26MPa. First, the difference between the fracture pressure and the pore pressure in the far field is lower in the case with $\bar{S}^{C}_{hmin}$=26 MPa compared with the other cases for which pumping pressures are quite similar (Fig. 12(a)). This pressure difference drives fluid leakoff from the fracture to the reservoir. Second, caprock fracturing leads the fracturing process in the low caprock stress case such that the fracture only penetrates into the reservoir a short distance, despite the larger overall height. In addition, the effective leakoff contact area is only a small fraction of the entire height of the reservoir. The combination of these factors determine that the low stress case has a lower leakoff coefficient and therefore a longer fracture length.

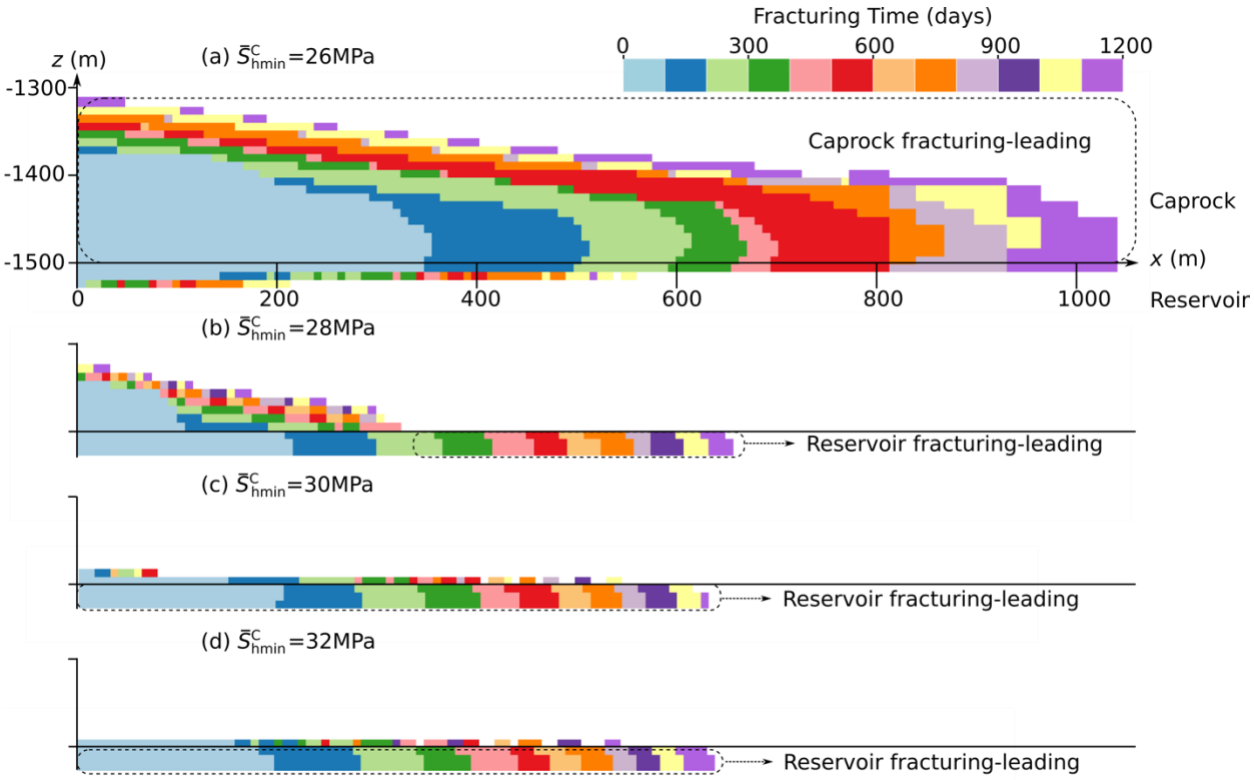

Fig. 11 Effect of the caprock *in situ* stress ((a) 26MPa, (b) 28MPa, (c) 30MPa, and (d) 32MPa on the distribution of fracturing time along the fracture. Quantities are projected onto the the *x*-*z* plane.

The magnitude of $\bar{S}^{C}_{hmin}$ also greatly affects the evolution of injection pressure and maximum aperture (Fig. 12). When $\bar{S}^{C}_{hmin}$ is sufficently high to contain fracturing mostly within the reservoir ($\bar{S}^{C}_{hmin}$=28, 30, 32 MPa), the injection pressure, as disucssed in the previous section, experiences first a plateau and then a gradual decline. However, when caprock fracturing leads the overall fracturing throughout the injection ($\bar{S}^{C}_{hmin}$=26 MPa), the injection pressure remains largely constant after the fracture grows into the caprock.

Fig. 12(b) shows that maximum apertures in all cases experience continuous increases. Cooling induced by CO_2 injection in the near wellbore region tends to play convoluted roles in affecting maximum apertures under different $\bar{S}^{C}_{hmin}$ levels. For a caprock fracturing-leading case

($\bar{S}^{C}_{hmin}$=26 MPa), the fracture-opening pressure, P^{o}_{f}, near the injection point, owing to the thermal-mechanical effect, could drop significantly. However, the fracture propagation pressure, P_p, which is dictated by the caprock *in situ* stress near the fracture front, remains largely unchanged (Fig. 12(a)), thereby causing a high net pressure. This high net pressure, in conjunction with the large overall fracture height, is likely to induce a large fracture aperture in the near-wellbore region. As shown in Fig. 12(b), the maximum aperture in the case with $\bar{S}^{C}_{hmin}$=26MPa reaches around 20 mm. Noticeably, this magnitude of maximum aperture far exceeds the value predicted by isothermal fracture models (McClure and Horne, 2014; Fu et al., 2017). Therefore, employing models that neglect the effects of thermo-elasticity for the simulation of fracturing in GCS will tend to underestimate the magnitude of fracture apertures.

For a reservoir fracturing-leading case ($\bar{S}^{C}_{hmin}$=28, 30, 32 MPa), however, the fracture opening pressure and the fracture propagation pressure both tend to decrease (Fig. 12(a)). In other words, there might not be a monotonic increase of net pressure at this region as it is in the case with $\bar{S}^{C}_{hmin}$=26 MPa, which explains a less remarkable increase of aperture magnitude. Meanwhile, the maximum apertures for cases with $\bar{S}^{C}_{hmin}$=30MPa and 32MPa approach similar values after 300 days of injection. This means in the long run, provided the caprock stress is high enough to prevent fracture propagation into the caprock, the exact magnitude does not play a significant role in affecting the system response.

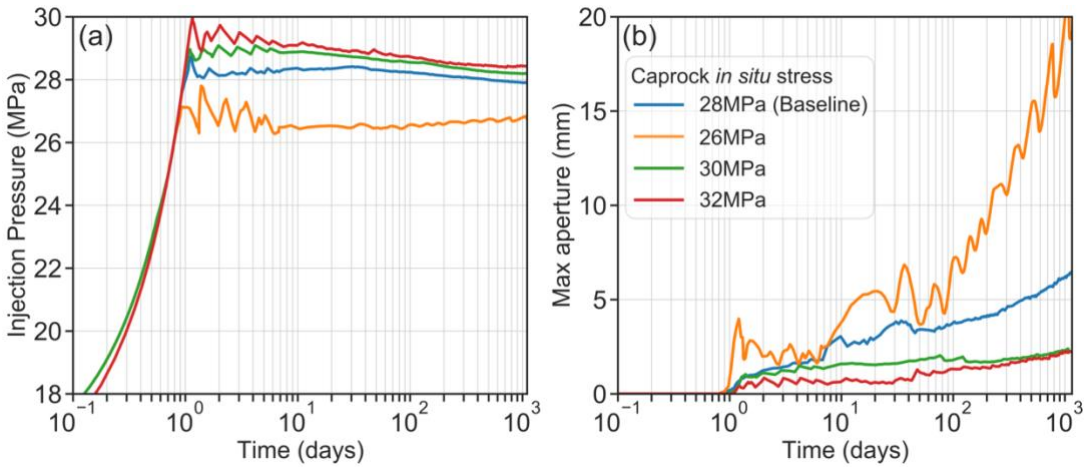

Fig. 12. Effect of the caprock *in situ* stress on (a) the injection pressure and (b) the maximum aperture. The apparent oscilation in the curves is caused by sudden pressure drop when the fracture propagates by the length of an element: a typical artifact for this type of space discretization scheme.

6 Concluding remarks

This paper develops an efficient and effective modeling scheme for simulating thermo-hydro-mechanical processes in fluid-driven fracturing. Such a modeling capability is crucial for studying geologic carbon storage (GCS) in reservoirs with marginal permeability where a hydraulic fracture could propagate in both the reservoir and caprock with complex phenomenology. The model captures multiphase multicomponent fluid flow and heat transfer within fractures and matrix, poro/thermo-mechanical deformation of solid rocks, and fracture propagation. Each of the physical processes is modeled using a robust individual module, and the modules are coupled utilizing a common simulation platform. In order to overcome the numerical challenges posed by coupling many complex processes, we take advantage of some self-stabilizing features of leakoff-dominated fracturing to simplify the numerical coupling. These features enable us to develop a sequential coupling scheme without convergence difficulties. Verification against the PKN solution in the leakoff-dominated regime indicates that

746 the simple scheme does not compromise the accuracy of the results for simulating leakoff-
747 dominated fracturing.

748 In simulating a 3D field-scale injection operation loosely based on the In Salah project, the
749 model reveals complex yet intriguing behaviors of the reservoir-caprock-fluid system. Soon after
750 the injection starts, back-stress caused by pressure diffusion in the reservoir drives a sharp
751 increase in injection pressure to keep the fracture open, until the pressure is high enough to drive
752 fracture propagation into the caprock. The injection pressure then remains largely constant at the
753 caprock's fracturing pressure. Injected fluid continued to be fed into the reservoir through the
754 slowly propagating fracture. Meanwhile, temperature decrease in the reservoir gradually reduces
755 the reservoir's total stress, and eventually the fracturing pressure of the reservoir becomes lower
756 than in the caprock. Thereafter the fracture mainly propagates in the reservoir, and the injection
757 pressure slowly declines accordingly. We also used the model to study the effects of the *in situ*
758 stress contrast between the reservoir and caprock on the vertical containment of the fracture.

759 We found many processes, including thermal, hydraulic, and mechanical processes, are involved
760 in fracturing caused by CO_2 injection. These processes have complex interactions and the
761 relative importance among these processes can evolve as injection progresses. The new model
762 proves effective in simulating these processes and their complex interactions in fidelity that is
763 unattainable for existing simple models. For example, thermal contraction induced by CO_2
764 injection has often been speculated to have a negative impact on fracture containment. Our study
765 shows that cold fluid injection itself could actually benefit the geomechanical containment of
766 fracturing under certain stress conditions within the caprock. Our results indicate that a gradual
767 pumping pressure decline can be used as a practical indicator of fracture growth during injection.

Despite the success in revealing the complex interactions among multiple physical processes, all the simulations presented in this paper used simplified stress profiles. More realistic stress profiles with layered fabric (Fisher and Warpinski, 2012) and "rough" in situ stress profiles (Fu et al., 2019), should be considered to further assess the caprock integrity and system responses in the future.

Acknowledge

This manuscript has been authored by Lawrence Livermore National Security, LLC under Contract No. DE-AC52-07NA2 7344 with the US. Department of Energy. The United States Government retains, and the publisher, by accepting the article for publication, acknowledges that the United States Government retains a non-exclusive, paid-up, irrevocable, world-wide license to publish or reproduce the published form of this manuscript, or allow others to do so, for United States Government purposes. This work is LLNL report LLNL-JRNL-816783.

Reference

Bohloli, B., Ringrose, P., Grande, L., Nazarian, B., 2017. Determination of the fracture pressure from CO_2 injection time-series datasets. Int. J. Greenh. Gas Control 61, 85–93. https://doi.org/10.1016/j.ijggc.2017.03.025

Brooks, R.H., Corey, A.T., 1964. Hydraulic Properties of Porous Media. Hydrology Papers 3. Colorado State University, Fort Collins, CO.

Bunger, A.P., Detournay, E., Garagash, D.I., 2005. Toughness-dominated hydraulic fracture with leak-off. Int. J. Fract. 134, 175–190. https://doi.org/10.1007/s10704-005-0154-0

Eshiet, K.I.I., Sheng, Y., 2014. Carbon dioxide injection and associated hydraulic fracturing of reservoir formations. Environ. Earth Sci. 72, 1011–1024. https://doi.org/10.1007/s12665-013-3018-3

Carrier, B., Granet, S., 2012. Numerical modeling of hydraulic fracture problem in permeable medium using cohesive zone model. Eng. Fract. Mech. 79, 312–328. https://doi.org/10.1016/j.engfracmech.2011.11.012

Coussy, O., 2004. Poromechanics. John Wiley and Sons, Chichester, England.

Culp, D., Tupek, M.R., Newell, P., Hubler, M.H., 2017. Phase-field modeling of fracture in CO_2 sequestration. In: 51st US Rock Mechanics/Geomechanics Symposium. American Rock Mechanics Association ARMA–2017–0644.

Fan, C., Elsworth, D., Li, S., Zhou, L., Yang, Z., Song, Y., 2019. Thermo-hydro-mechanical-chemical couplings controlling CH4 production and CO_2 sequestration in enhanced coalbed methane recovery. Energy 173, 1054–1077. https://doi.org/10.1016/j.energy.2019.02.126

Fu, P., Johnson, S.M., Carrigan, C.R., 2013. An explicitly coupled hydro-geomechanical model for simulating hydraulic fracturing in arbitrary discrete fracture networks. Int. J. Numer. Anal. Methods Geomech. 37, 2278–2300. https://doi.org/10.1002/nag.2135

Fu, P., Settgast, R.R., Hao, Y., Morris, J.P., Ryerson, F.J., 2017. The Influence of Hydraulic Fracturing on Carbon Storage Performance. J. Geophys. Res. Solid Earth 122, 9931–9949. https://doi.org/10.1002/2017JB014942

Fu, P., Huang, J., Settgast, R.R., Morris, J.P., Ryerson, F.J., 2019. Apparent toughness anisotropy induced by "roughness" of in-situ stress: A mechanism that hinders vertical growth of hydraulic fractures and its simplified modeling. SPE J. 24, 2148–2162. https://doi.org/10.2118/194359-PA

Fu, P., Ju, X., Huang, J., Settgast, R. R., Morris, J. P., 2019. THM Modeling of Poroelastic Sustainability of Hydraulic Fracture in CO_2 Storage Reservoirs. In American Rock Mechanics Association. In *Proceedings of the 44th US Rock Mechanics Symposium*, New York, NY, ARMA-2019-1601, 2019.

Fu, P., Ju, X., Huang, J., Settgast, R.R., Liu, F., Morris, J.P., 2020. Thermo-poroelastic responses of a pressure-driven fracture in a carbon storage reservoir and the implications for injectivity and caprock integrity. Int. J. Numer. Anal. Methods. Geomech. 1–19. https://doi.org/10.1002/nag.3165

Francfort, G.A., Bourdin, B., Marigo, J.J., 2008. The variational approach to fracture, Journal of Elasticity. https://doi.org/10.1007/s10659-007-9107-3

Francfort, G.A., Marigo, J.-J., 1998. Revisiting brittle fracture as an energy minimization problem. J. Mech. Phys. Solids 46, 1319–1342. https://doi.org/10.1016/S0022-5096(98)00034-9

Fisher, K., Warpinski, N., 2012. Hydraulic-fracture-height growth: Real data. SPE Prod. Oper. 27, 8–19. https://doi.org/10.2118/145949-pa

827 Garagash, D.I., Detournay, E., Adachi, J.I., 2011. Multiscale tip asymptotics in hydraulic fracture
828 with leak-off. J. Fluid Mech. 669, 260–297. https://doi.org/10.1017/S002211201000501X

829 Gheibi, S., Vilarrasa, V., Holt, R.M., 2018. Numerical analysis of mixed-mode rupture
830 propagation of faults in reservoir-caprock system in CO_2 storage. Int. J. Greenh. Gas Control 71,
831 46–61. https://doi.org/10.1016/j.ijggc.2018.01.004

832 Girault, V., Kumar, K., Wheeler, M.F., Wheeler, M.F., 2016. Convergence of iterative coupling
833 of geomechanics with flow in a fractured poroelastic medium. Comput. Geosci. 997–1011.
834 https://doi.org/10.1007/s10596-016-9573-4

835 Guo, B., Tao, Y., Bandilla, K., Celia, M., 2017. Vertically Integrated Dual-porosity and Dual-
836 permeability Models for CO_2 Sequestration in Fractured Geological Formation. Energy Procedia
837 114, 3343–3352. https://doi.org/10.1016/j.egypro.2017.03.1466

838 Gor, G.Y., Elliot, T.R., Prevost, J.H., 2013. Effects of thermal stresses on caprock integrity
839 during CO_2 storage. Int. J. Greenh. Gas Control 12, 300–309.

840 Haszeldine, R.S., 2009. Carbon Capture and Storage: How Green Can Black Be? Science. 325,
841 1647–1652. https://doi.org/10.1126/science.1172246

842 Huang, J., Fu, P., Settgast, R.R., Morris, J.P., Ryerson, F.J., 2019. Evaluating a Simple
843 Fracturing Criterion for a Hydraulic Fracture Crossing Stress and Stiffness Contrasts. Rock
844 Mech. Rock Eng. 52, 1657–1670. https://doi.org/10.1007/s00603-018-1679-7

Iding, M., Ringrose, P., 2010. Evaluating the impact of fractures on the performance of the In Salah CO_2 storage site. Int. J. Greenh. Gas Control 4, 242–248. https://doi.org/10.1016/j.ijggc.2009.10.016

International Energy Agency. Energy Technology Perspectives 2010: Scenarios and Strategies to 2050; 2010; International Energy Agency, Paris, France.

Ju, X., Liu, F., Fu, P., D. White, M., R. Settgast, R., P. Morris, J., 2020. Gas Production from Hot Water Circulation through Hydraulic Fractures in Methane Hydrate-Bearing Sediments: THC-Coupled Simulation of Production Mechanisms. Energy & Fuels 0. https://doi.org/10.1021/acs.energyfuels.0c00241

Kim, J., Tchelepi, H.A., Juanes, R., 2011. Stability and convergence of sequential methods for coupled flow and geomechanics: Fixed-stress and fixed-strain splits. Comput. Methods Appl. Mech. Eng. 200, 1591–1606. https://doi.org/10.1016/j.cma.2010.12.022

Kim, J., Moridis, G., Yang, D., Rutqvist, J., 2012. Numerical Studies on Two-Way Coupled Fluid Flow and Geomechanics in Hydrate Deposits. SPE J. 17, 485–501. https://doi.org/10.2118/141304-PA

Kim, J., Moridis, G.J., 2013. Development of the T+M coupled flow-geomechanical simulator to describe fracture propagation and coupled flow-thermal-geomechanical processes in tight/shale gas systems. Comput. Geosci. 60, 184–198. https://doi.org/10.1016/j.cageo.2013.04.023

Howard, G.C., Fast, C., 1957. Optimumfluid characteristics for fracture extension. Drill. Prod. Prac. 24, 261–270.

865 Li, Z. and Elsworth, D., 2019. Controls of CO_2–N_2 gas flood ratios on enhanced shale gas
866 recovery and ultimate CO_2 sequestration. J. Pet. Sci. Eng. 179, 1037-1045.

867 Lecampion, B., Bunger, A., Zhang, X., 2018. Numerical methods for hydraulic fracture
868 propagation: A review of recent trends. J. Nat. Gas Sci. Eng. 49, 66–83.
869 https://doi.org/10.1016/j.jngse.2017.10.012

870 McClure, M.W., Horne, R.N., 2014. An investigation of stimulation mechanisms in Enhanced
871 Geothermal Systems. Int. J. Rock Mech. Min. Sci. 72, 242–260.
872 https://doi.org/10.1016/j.ijrmms.2014.07.011

873 Mito, S., Xue, Z., Ohsumi, T., 2008. Case study of geochemical reactions at the Nagaoka CO_2
874 injection site, Japan. Int. J. Greenhouse Gas Control 2, 309–318.

875 Moridis, G.J., Freeman, C.M., 2014. The RealGas and RealGasH2O options of the TOUGH+
876 code for the simulation of coupled fluid and heat flow in tight/shale gas systems. Comput.
877 Geosci. 65, 56–71. https://doi.org/10.1016/j.cageo.2013.09.010

878 Morris, J.P., Hao, Y., Foxall, W., McNab, W., 2011. A study of injection-induced mechanical
879 deformation at the In Salah CO_2 storage project. Int. J. Greenh. Gas Control 5, 270–280.
880 https://doi.org/10.1016/j.ijggc.2010.10.004

881 Mollaali, M., Ziaei-Rad, V., Shen, Y., 2019. Numerical modeling of CO_2 fracturing by the phase
882 field approach. J. Nat. Gas Sci. Eng. 70, 102905. https://doi.org/10.1016/j.jngse.2019.102905

883 Nordgren, R.P., 1972. Propagation of a Vertical Hydraulic Fracture. Soc. Pet. Eng. J. 12, 306–
884 314. https://doi.org/10.2118/3009-pa

885 Orr, F.M., 2009. Onshore geologic storage of CO_2. Science. 325, 1656–1658.
886 https://doi.org/10.1126/science.1175677

887 Oye, V., Aker, E., Daley, T.M., Kühn, D., Bohloli, B., Korneev, V., 2013. Microseismic
888 monitoring and interpretation of injection data from the In Salah CO_2 storage site (Krechba),
889 Algeria. Energy Procedia 37, 4191–4198. https://doi.org/10.1016/j.egypro.2013.06.321

890 Pacala, S., Socolow, R, 2004. Stabilization Wedges: Solving the Climate Problem for the Next
891 50 Years with Current Technologies. Science. 305, 968–972.
892 https://doi.org/10.1126/science.1100103

893 Paluszny, A., Graham, C.C., Daniels, K.A., Tsaparli, V., Xenias, D., Salimzadeh, S., Whitmarsh,
894 L., Harrington, J.F., Zimmerman, R.W., 2020. Caprock integrity and public perception studies of
895 carbon storage in depleted hydrocarbon reservoirs. Int. J. Greenh. Gas Control 98, 103057.
896 https://doi.org/10.1016/j.ijggc.2020.103057

897 Pan, L., Oldenburg, C.M., Pruess, K., Wu, Y.-S., 2011. Transient CO_2 leakage and injection in
898 wellbore-reservoir systems for geologic carbon sequestration. Greenh. Gases Sci. Technol. 1,
899 335–350. https://doi.org/10.1002/ghg.41

900 Perkins, T.K., Kern, L.R., 1961. Widths of Hydraulic Fractures. J. Pet. Technol. 13, 937–949.
901 https://doi.org/10.2118/89-pa

902 Raziperchikolaee, S., Alvarado, V., Yin, S., 2013. Effect of hydraulic fracturing on long-term
903 storage of CO_2 in stimulated saline aquifers. Appl. Energy 102, 1091–1104.
904 https://doi.org/10.1016/j.apenergy.2012.06.043

905 Ren, F., Ma, G., Wang, Y., Fan, L., Zhu, H., 2017. Two-phase flow pipe network method for
906 simulation of CO_2 sequestration in fractured saline aquifers. Int. J. Rock Mech. Min. Sci. 98, 39–
907 53. https://doi.org/10.1016/j.ijrmms.2017.07.010

908 Rinaldi, A.P., Rutqvist, J., 2013. Modeling of deep fracture zone opening and transient ground
909 surface uplift at KB-502 CO_2 injection well, In Salah, Algeria. Int. J. Greenh. Gas Control 12,
910 155–167. https://doi.org/10.1016/j.ijggc.2012.10.017

911 Ringrose, P.S., Mathieson, A.S., Wright, I.W., Selama, F., Hansen, O., Bissell, R., Saoula, N.,
912 Midgley, J., 2013. The in salah CO_2 storage project: Lessons learned and knowledge transfer.
913 Energy Procedia 37, 6226–6236. https://doi.org/10.1016/j.egypro.2013.06.551

914 Rutqvist, J., Vasco, D.W., Myer, L., 2010. Coupled reservoir-geomechanical analysis of CO_2
915 injection and ground deformations at In Salah, Algeria. Int. J. Greenh. Gas Control 4, 225–230.
916 https://doi.org/10.1016/j.ijggc.2009.10.017

917 Pruess, K., Tsang, Y.W., 1990. On two-phase relative permeability and capillary pressure of
918 rough-walled rock fractures. Water Resour. Res. 26, 1915–1926.
919 https://doi.org/10.1029/WR026i009p01915

920 Rutqvist, J., Rinaldi, A.P., Cappa, F., Moridis, G.J., 2013. Modeling of fault reactivation and
921 induced seismicity during hydraulic fracturing of shale-gas reservoirs. J. Pet. Sci. Eng. 107, 31–
922 44. https://doi.org/10.1016/j.petrol.2013.04.023

923 Salimzadeh, S., Paluszny, A., Zimmerman, R.W., 2017. Three-dimensional poroelastic effects
924 during hydraulic fracturing in permeable rocks. Int. J. Solids Struct. 108, 153–163.
925 https://doi.org/10.1016/j.ijsolstr.2016.12.008

926 Salimzadeh, S., Paluszny, A., Zimmerman, R.W., 2018. Effect of cold CO_2 injection on fracture
927 apertures and growth. Int. J. Greenh. Gas Control 74, 130–141.
928 https://doi.org/10.1016/j.ijggc.2018.04.013

929 Salimzadeh, S., Hagerup, E.D., Kadeethum, T., Nick, H.M., 2019. The effect of stress
930 distribution on the shape and direction of hydraulic fractures in layered media. Eng. Fract. Mech.
931 215, 151–163. https://doi.org/10.1016/j.engfracmech.2019.04.041

932 Senseny, P.E., Pfeifle, T.W., 1984. Fracture toughness of sandstones and shales. In: The 25th US
933 Symposium on Rock Mechanics (USRMS). 25–27 June, Evanston Illinois.

934 Settgast, R.R., Fu, P., Walsh, S.D.C., White, J.A., Annavarapu, C., Ryerson, F.J., 2016. A fully
935 coupled method for massively parallel simulation of hydraulically driven fractures in 3-
936 dimensions. Int. J. Numer. Anal. Methods Geomech. https://doi.org/10.1002/nag.2557

937 Sun, Z., Espinoza, D.N., Balhoff, M.T., 2016. Discrete element modeling of indentation tests to
938 investigate mechanisms of CO_2-related chemomechanical rock alteration. J. Geophys. Res. Solid
939 Earth 121, 7867–7881. https://doi.org/10.1002/2016JB013554

940 Sun, Z., Espinoza, D.N., Balhoff, M.T., Dewers, T.A., 2017. Discrete Element Modeling of
941 Micro-scratch Tests: Investigation of Mechanisms of CO_2 Alteration in Reservoir Rocks. Rock
942 Mech. Rock Eng. 50, 3337–3348. https://doi.org/10.1007/s00603-017-1306-z

Vilarrasa, V., Olivella, S., Carrera, J., Rutqvist, J., 2014. Long term impacts of cold CO_2 injection on the caprock integrity. Int. J. Greenh. Gas Control 24, 1–13. https://doi.org/10.1016/j.ijggc.2014.02.016

Vilarrasa, V., Laloui, L., 2015. Potential fracture propagation into the caprock induced by cold CO_2 injection in normal faulting stress regimes. Geomech. Energy Environ. 2, 22–31.

Vilarrasa, V., Rinaldi, A.P., Rutqvist, J., 2017. Long-term thermal effects on injectivity evolution during CO_2 storage. Int. J. Greenh. Gas Control 64, 314–322. DOI: 10.1016/j.ijggc.2017.07.019

White, J.A., Chiaramonte, L., Ezzedine, S., Foxall, W., Hao, Y., Ramirez, A., McNab, W., 2014. Geomechanical behavior of the reservoir and caprock system at the In Salah CO_2 storage project. Proc. Natl. Acad. Sci. 111, 8747–8752. https://doi.org/10.1073/pnas.1316465111

White, J.A., Castelletto, N., Tchelepi, H.A., 2016. Block-partitioned solvers for coupled poromechanics: A unified framework. Comput. Methods Appl. Mech. Eng. 303, 55–74. https://doi.org/10.1016/j.cma.2016.01.008

Witherspoon, P.A., Wang, J.S.Y., Iwai, K., Gale, J.E., 1980. Validity of Cubic Law for fluid flow in a deformable rock fracture. Water Resour. Res. 16, 1016–1024. https://doi.org/10.1029/WR016i006p01016

Yan, H., Zhang, J., Zhou, N., Li, M., Suo, Y., 2020. Numerical simulation of dynamic interactions between two cracks originating from adjacent boreholes in the opposite directions during supercritical CO_2 fracturing coal mass. Eng. Fract. Mech. 223, 106745. https://doi.org/10.1016/j.engfracmech.2019.106745

963 Van Genuchten, M.T., 1980. A closed-form equation for predicting the hydraulic conductivity of
964 unsaturated soils. Soil Sci. Soc. Am. J. 44 (5), 892–898.